



1 **StageIV-IRC: A High-resolution Dataset of Extreme Orographic Quantitative**
2 **Precipitation Estimates (QPE) Constrained to Water Budget Closure for**
3 **Historical Floods in the Appalachian Mountains**

4 Mochi Liao¹ and Ana P. Barros¹

5 1. Civil and Environmental Engineering, University of Illinois Urbana-
6 Champaign, Urbana, IL

7 **Corresponding Author:**

8 Dr. Ana Barros

9 E-mail: barros@illinois.edu

10 Phone: +1 217-333-8038

11



12 **Abstract**

13 Quantitative Flood Estimation (QFE) in complex terrain remains a grand challenge in
14 operational hydrology due to the lack of accurate high-resolution Quantitative Precipitation
15 Estimates (QPE) for operational forecasting and for calibrating hydrologic models. Here, we
16 present a high-resolution (i.e., 250m, 5-minute-hourly) QPE dataset for 215 extreme rainfall events
17 occurred in 26 gauged mountainous basins in the Appalachian Mountains from 2008 to 2024. This
18 dataset is developed by applying inverse rainfall corrections (IRC) derived from physically-based
19 rainfall-runoff modeling (Liao and Barros, 2022 and 2023) to the Next Generation Weather Radar
20 (NEXRAD) Stage IV analysis (4 km resolution, hourly). The corrected Stage IV analysis QPE is
21 referred to as StageIV-IRC (StageIV with Inverse Rainfall Correction). The unique advantage of
22 this StageIV-IRC QPE dataset is its agreement with ground-based rainfall measurements while
23 achieving water budget closure at the storm-flood event scale within observational uncertainty of
24 streamflow observations, which is the gold standard in hydrological modeling. This dataset is the
25 first QPE dataset aiming to improve QFE in the complex terrain by reducing biases for extreme
26 precipitation events, and it can be used to evaluate the skill of hydrologic models in the same basins
27 and support model calibration. The StageIV-IRC QPE dataset is publicly available at
28 <https://doi.org/10.5281/zenodo.14028866>, and improved initial soil moisture maps for the studied
29 extreme precipitation events, derived from the same IRC framework, are available in the same
30 repository (Liao and Barros, 2025c).

31



32 1. Introduction

33 Over the past few decades, extreme precipitation has become an increasingly important
34 research topic due to its social, economic, and environmental impacts (e.g., Alimonti et al., 2022;
35 Wernberg et al., 2013). Studies show that both total annual precipitation and extreme precipitation
36 events have increased in the US and in other parts of the world during the last century (e.g., Milly
37 et al., 2002), often resulting in floods (e.g., Pielke and Downton, 2002), and flash floods in the
38 context of complex terrain due to steep slopes (e.g., Schumacher, 2017; Czigány et al., 2010).
39 Flash floods are characterized by fast rainfall-runoff responses on the scale of a few hours (< 6
40 hours) after extreme precipitation events for watershed areas often ranging from a few tens to
41 hundreds of square kilometers (e.g., Borga et al., 2014; Lumbroso and Gaume, 2012). As one of
42 the deadliest natural hazards, flash floods are often associated with landslide events (e.g., Tao and
43 Barros, 2014; Gupta et al., 2016; Deijns et al., 2022) and cause loss of life and property damage
44 (Špitalar et al., 2014), such as recently in the last three years in the Appalachian Mountains, USA,
45 and in Southern Spain. Despite extensive studies to improve flash flood simulations in small
46 headwater basins, hydrological skill scores (e.g., Kling-Gupta Efficiency or KGE) remain poor at
47 event scales largely due to significant difficulties involved in estimating highly localized
48 orographic precipitation in complex terrain, which in turn implies that hydrologic models are not
49 calibrated using forcing representative of realistic extreme events (e.g., Andrieu et al. 1997;
50 Huffman et al., 2007; Mtibaa and Asano, 2022).

51 Current approaches involved in precipitation measurement and Quantitative Precipitation
52 Estimation (i.e., QPE) broadly include in-situ point-scale observations using rain gauges and
53 disdrometers, and remote spatial observations using ground-based radar and space-based sensors.
54 In complex terrain, there is often a scarcity of in situ measurements due to difficult access. For



55 example, the rain gauge network from NASA's Integrated Precipitation and Hydrology Experiment
 56 is the only relatively dense rain gauge network installed at high elevations in the entire
 57 Appalachians (e.g., Barros et al. 2014). Other QPE products (e.g., radar QPE data) are plagued by
 58 uncertainties from various sources (e.g., ground clutter artifacts, retrieval uncertainties, and radar
 59 viewing geometry (Villarini and Krajewski, 2010; Arulraj and Barros, 2021; Kreklow et al., 2020;
 60 Huffman et al., 2007; Andrieu et al., 1997; Durden et al., 1998). Numerical weather prediction
 61 (NWP) is an alternative to measurement. However, QPE products from NWP models are
 62 characterized by significant uncertainties when evaluated against rain gauges (e.g., Zhang and
 63 Anagnostou, 2019), leading to large flood simulation errors when used as inputs to hydrological
 64 models, or introducing large structural uncertainty when used for model calibration (e.g., Tao et
 65 al., 2016; Weiland et al., 2015; Diomede et al., 2008; Kobold and Suselj, 2005). Due to these
 66 uncertainties and errors involved, focus has been directed towards enhancing QPE using various
 67 methods: data merging of raingauge and radar precipitation (e.g., McKee and Binns, 2016;
 68 Goudenhoofdt and Delobbe, 2009; Delrieu et al., 2014; Nanding et al., 2015; Sideris et al. 2013;
 69 Schiemann et al. 2011), combined radar reflectivity and retrieval corrections (e.g., Vignal et al.,
 70 2000; Shao et al., 2021; Dinku et al., 2002), and data assimilation into NWP models (e.g.,
 71 Rafieeinasab et al., 2015; Wehbe et al., 2020). Rain gauge and disdrometer measurements are often
 72 used as references for these QPE optimization approaches (e.g., Harrison et al., 2000; Shao et al.,
 73 2021; Fulton et al., 1998). The 'ground truth', however, has its own error (e.g., spatial
 74 representativeness, wind artifacts around the gauge orifice, and calibration, among others;
 75 Kochendorfer et al., 2017), and fails to capture highly localized orographic enhancement (e.g., Prat
 76 and Barros, 2010b; Gentilucci et al., 2021; Buytaert et al., 2006). Gauge-radar fusion often relies
 77 on geostatistical assumptions that are primarily distance-based (e.g., Areerachakul et al., 2022;



78 Cassiraga et al., 2021; Wang et al., 2020; Maggioni and Massari, 2018), lacking the full picture of
79 complex basin topography, which has a regulating role in orographic precipitation processes.

80 To address this long-standing QPE challenge in complex terrain, a general QPE error
81 quantification framework was developed leveraging widely available quality United States
82 Geological Survey (USGS) streamflow observations at the outlet of headwater basins in complex
83 terrain, consisting of 2 distinct paths: 1) rain gauge bias correction, and 2) grid-level QPE
84 correction constrained to watershed-scale water budget closure. The first pathway includes rain
85 gauge bias corrections at gauge locations both at the diurnal and climate scales, and the
86 geostatistical distribution of rain gauge biases across a basin. The second pathway includes an
87 innovative inverse QPE correction method by backward propagating runoff uncertainty using a
88 hydrological model via streamlines to precipitation at storm-event scale, and the methodology is
89 termed Inverse Rainfall Correction (IRC), which is developed by the same authors (Liao and
90 Barros, 2022 or LB22).

91 LB22 found that initial soil moisture uncertainty causes inferior performance of IRC
92 because large initial condition errors lead to significant uncertainties in travel time distributions.
93 Soil moisture is considered a particularly important factor among soil properties due to its
94 significant role in affecting the generation of runoff, hence dramatically altering the timing of flood
95 front and its magnitudes (e.g., Vivoni et al., 2007; Marchi et al., 2010; Penna et al., 2011), and soil
96 moisture can vary dramatically at hourly timescales, changing from fully saturation levels to
97 wilting point levels conditional on the specific texture and other properties of the soils (Grillakis
98 et al., 2016). Initial soil moisture conditions can therefore determine whether a rainstorm produces
99 a major flash flood or not (e.g., Komma et al., 2007; Zehe and Blöschl, 2004). However, due to
100 the limited availability of soil moisture sensors, there are not many studies quantifying the impact



101 of soil moisture on runoff simulation (e.g., Silvestro et al., 2019; Laiolo et al., 2016; Zappa et al.,
 102 2011; Uber et al., 2018). Liao and Barros (2025b) developed an Initial Condition Correction (ICC),
 103 which is based on travel time distributions and is coupled with the general IRC approach,
 104 demonstrating large improvements in initial soil moisture estimation. Note that when
 105 implementing the IRC and ICC, we are using a fully distributed physics-based uncalibrated model
 106 (i.e. Duke Coupled Hydrological Model, DCHM) that has been used successfully for more than
 107 two decades for hydrologic studies in the Southern and Central Appalachians (e.g., Tao and Barros,
 108 2013, 2014, 2018 and 2019; Tao et al. 2016; Yildiz and Barros 2004, 2007 and 2009), and
 109 consequently uncertainty from model structure and model parameters is assumed to be small.
 110 Hydrological model parameters certainly have an impact on rainfall-runoff response, but they are
 111 generally only of secondary importance compared to the precipitation proper and antecedent soil
 112 moisture distributions, especially for smaller basins (e.g., Dobler et al., 2012; Mockler et al., 2016).

113 In this work, IRC and ICC are combined into one structure (referred to as the IRC-ICC
 114 framework) to construct an improved QPE dataset aiming to close the water budget at the scale of
 115 storm-flood events along the entire Appalachian Mountains (e.g., Liao and Barros 2022 and
 116 2025b). The study region is set to be the Appalachian Mountains because they are prone to extreme
 117 precipitation and flash floods due to orographic lift of moisture-laden air masses coming from the
 118 Gulf of Mexico and the Atlantic Ocean (e.g., Troch et al., 1994; Smith et al., 2011; Liao and
 119 Barros, 2023). A recent example is Hurricane Helene, which caused over 200 deaths and over \$50
 120 billion in property damage in the Southeast US in September 2024. The IRC-ICC framework is
 121 employed in 26 headwater basins and 215 extreme events (during 2008-2024) using the Next
 122 Generation Weather Radar (NEXRAD) StageIV dataset as original inputs, at a spatial and temporal



123 resolution of 250 m and 5 minutes, respectively, and the improved post IRC-ICC QPE data (i.e.,
124 StageIV-IRC) are made available in this study.

125 The manuscript is organized as follows. The data sources and the QPE error quantification
126 framework, which consists of rain gauge bias correction and the IRC-ICC framework, are detailed
127 in Section 2. Section 3 presents this new dataset (StageIV-IRC) along with data assessment from
128 various aspects. Section 4 discusses the potential application of this new dataset and future work.
129 Section 5 provides access to the dataset and a summary of the work.

130

131 **2. Data and Methodology**

132 **2.1 Radar QPE StageIV**

133 The NCEP/EMC StageIV is a precipitation estimation product, developed using hourly and
134 6-hourly radar-raingauge precipitation analyses at regional scales (Lin and Mitchell, 2005). In
135 complex terrain, it is known that radar QPE suffers from the blockage of topography, overshooting
136 and retrieval uncertainties, leading to large uncertainties in rainfall estimation. In 2007, as part of
137 the ground validation (GV) of the Precipitation Measurement Missions (PMM) program by NASA
138 (e.g., Prat and Barros, 2010a and 2010b), 34 tipping bucket raingauges were installed in the
139 Southern Appalachians and have been well-maintained since 2007 (e.g., Barros et al., 2014). In
140 this work, raingauge measurements from a GV raingauge network in the Southern Appalachians
141 are utilized to reduce StageIV uncertainties.

142 **2.2 GV Rain Gauge Observations**

143 A rain gauge network in support of PMM GV was installed in the Pigeon River basin for
144 the 10 year 2007-2018 period (Barros et al. 2014). A map of this rain gauge network is plotted in



145 Figure 1. Every rain gauge is labelled with a number, and exact locations are documented in Table
146 1. This rain gauge network is regularly visited and maintained at least three times a year, including
147 on-site cleaning and calibration. In this study, these rainfall measurements are used as a basis to
148 adjust hourly StageIV QPE. Note these rain gauge measurements can be downloaded at
149 <http://dx.doi.org/10.5067/GPMGV/IPHEX/GAUGES/DATA301> (Barros et al., 2017). Besides
150 rain gauges, a network of Parsivel disdrometers was installed during 2013-2014, with each
151 disdrometer location denoted by the letter P in Figure 1. These disdrometer data were only used
152 for independent evaluation because of short records. It is worth noting that rain gauges are installed
153 mostly along the ridges while disdrometers are generally located at lower elevations.

154

155 <Figure 1 here please>

156

157 **2.3 Methodology**

158 The methodology of this work includes three major components: 1) rain gauge bias
159 correction, 2) grid-scale QPE correction by closing the water budget using stream gauge
160 measurements, and 3) basin and event selection procedures and model setup.

161 **2.3.1 Rain gauge Bias Correction**

162 A schematic drawing of the rain gauge bias correction framework to derive gauge-
163 improved QPE (named StageIV_{DBKC}) is provided in Figure 2.

164 <Figure 2 here please>

165



166 First, to make meaningful comparison between StageIV and rain gauges in space, a fractal
 167 downscaling algorithm is used to create StageIV_D at 1km from the original StageIV at 4 km
 168 resolution. Subsequently, bias correction using raingauge measurements is employed to create
 169 StageIV_{DB} at hourly timescales. StageIV_{DB} data are then evaluated against the rain gauge
 170 climatology from 2008 to 2017 to reduce biases that depend on weather regime, and climatological
 171 biases are then interpolated using the ordinary Kriging method. The resulting dataset is named
 172 StageIV_{DBKC} (abbreviated as STIV_{DBKC}).

173

174 2.3.2 Fractal downscaling

175 The methodology for fractal downscaling was first proposed by Bindlish and Barros (1996)
 176 and subsequently demonstrated through various applications to precipitation downscaling from
 177 models (Bindlish and Barros, 2000) and remote sensing data (Nogueira and Barros, 2015; Tao and
 178 Barros, 2010). Here, a brief description is presented.

179 The assumption of self-similarity is imposed in fractal downscaling approach. The
 180 parameters used in this approach involve: fractal dimension D , Hurst coefficient H , and the spectral
 181 exponent β that are related through the following equations:

$$182 \quad D = \frac{7-\beta}{2} \quad (1)$$

$$183 \quad H = \frac{\beta-1}{2} \quad (2)$$

184 The parameter β describes rainfall statistics across different spatial scales, and it is
 185 calculated as the slope of the power spectral density curve in the 2D Fourier domain of the rainfall
 186 field (log-log plot). The parameter H is the Hurst coefficient which is a measure of autocorrelation



187 strength with higher value representing stronger autocorrelation. The power spectral density of a
 188 2D field in Fourier domain is calculated as the following:

$$189 \quad Z(u, v) = \left(\frac{L}{N}\right)^2 \sum_{x=0}^{N-1} \sum_{y=0}^{N-1} z(x, y) \exp\left[-\frac{2\pi i}{N}(ux + vy)\right] \quad (3)$$

190 where N is the total number of grid points of the rainfall field $z(x, y)$ with grid size being
 191 the L , u and v correspond to frequency indices in the Fourier domain in each direction. The
 192 averaged power spectral density is given:

$$193 \quad S_j = \frac{1}{L^2 N_j} \sum_1^{N_j} |Z(u, v)|^2 \quad (4)$$

194 where N_j denotes the number of points that meet the following condition: $j < \sqrt{u^2 + v^2} <$
 195 $j + 1$. There is roughly a power-law relationship between the wavenumber k and the mean power
 196 spectral density, and k is defined as below:

$$197 \quad k = \frac{2\pi}{\sqrt{u^2 + v^2}} \quad (5)$$

$$198 \quad S \sim k^{-\beta-1} \quad (6)$$

199 Specifically, the corresponding S value when wavenumber $k = 1$ is referred to as the
 200 roughness factor, which is a representation of the variance of the field.

201 Assuming rainfall fields have self-similar statistics from coarse resolution to fine
 202 resolution, then fine scale rainfall fields can be generated by preserving these self-similar statistics.
 203 This is accomplished by creating a Brownian surface at desired fine scale resolution while sharing
 204 the same spectral slope and roughness factor as the original rainfall field based on Bindlish and
 205 Barros (1996):



$$Z_D(u, v) = \frac{Z_b(u, v)}{k_r^{(\beta - \beta_b)/2}} \exp \left[\frac{1}{2} \left(S_{r,1} - \frac{\beta + 1}{\beta_b + 1} S_{r,2} \right) \right] \quad (7)$$

where β , β_b , $Z_D(u, v)$ and $Z_b(u, v)$ are the spectral slope of 2D original rainfall field, the spectral slope of the Brownian surface, interpolation surface in the Fourier domain and original Brownian surface, respectively; k_r is the wavenumber and $S_{r,1}$ and $S_{r,2}$ are the roughness factors of the 2D original rainfall fields and Brownian surface. Due to the non-uniqueness of Brownian surfaces, multiple replicates of interpolation surfaces Z_D can be obtained. In this study, an ensemble of ND interpolation surfaces is derived, thus ND rainfall fields at finer resolution preserving the same rainfall statistics at coarse resolution are generated. In this work, a total of ND=50 ensemble downscaled rainfall fields are created similar to Nogueira and Barros (2015), and a series of rainfall bias correction steps is described in Figure 2 and is applied to the ensemble mean of the downscaled rainfall fields.

217

2.3.3 Bias Correction

The first phase of bias correction is carried out at the event scale: a linear regression is established between rain gauge measurements and collocated downscaled radar pixel estimates using the following formula:

$$R_g^t(i_g, j_g) = \kappa R_r^t(i_g, j_g) + \varepsilon \quad (8)$$

where R_r and R_g represent radar and rain gauge measurements respectively, κ and ε are the slope and the intercept of a polynomial fit between R_r and R_g . Hourly StageIV_D estimates and corresponding rain gauge observations in the same StageIV_D pixel were identified if at least 2 rain gauges in the same StageIV_D pixel measure non-zero rainfall. A linear regression was applied to



all StageIV_D pixels within one standard deviation of the regression line at an hourly timescale by assuming homogeneity of variances or homoscedasticity.

The second phase of bias correction is done at decadal scale: aiming to reduce systematic radar errors caused by retrieval uncertainties and viewing geometry in complex terrain, demonstrating strong diurnal (time of day) and seasonal (weather regime) error dependencies due to miss detection of shallow rainfall systems related to radar overshooting in the Southern Appalachian when comparing against 10-year rain gauge observations (e.g., Wilson and Barros, 2014; Arulraj and Barros, 2017). For this purpose, when rain gauge observations are <2mm/hr and Stage IV_D estimates are 0mm/hr, the StageIV_D value was automatically replaced by the rain gauge observations, which is referred to as the Light Rainfall Correction (LRC). Moreover, if StageIV_D estimates equal to 0 where at least one collocated rain gauge observation is >2mm/hr, then StageIV_D estimates are replaced by the mean of all collocated rain gauge observations, namely Mean Rainfall Correction (MRC). Lastly, for highly localized precipitation (i.e., less than 2 rainguages register nonzero rain in the study domain) which is normally produced by convective activity, the rainfall differences between the StageIV_D and the local rain gauge observations were bilinearly distributed across nearby 25 grids (a 5x5 grid square centered at the StageIV_D pixel)– Convective Rainfall Correction (CRC). For most of the raining hours, there are more than 2 rain gauges recorded rain, in which case the differences at each pixel between radar estimates and raingauge measurements were spatially interpolated using a geostatistical interpolation method (e.g., ordinary Kriging), which is referred to as the Global Rainfall Correction (GRC).



248 2.3.4 Ordinary Kriging

249 Ordinary Kriging is a geostatistical interpolation method that generates artificial values of
 250 a variable at a specific location, aiming to minimize spatial variance. In this work, rainfall
 251 differences between raingauge observations and StageIV_{DB} are calculated and distributed across
 252 the entire basin using a spatial variance model, which is commonly referred to as a semi-variogram
 253 model. Specifically, a spherical semi-variogram model is used. Literature regarding the choice of
 254 semi-variogram models and their properties can be found (e.g., Li and Heap, 2008; Oliver and
 255 Webster, 2015; Zimmerman and Zimmerman, 1991). Bohling (2005) pointed out that spherical
 256 models reach the maximum variance for relatively shorter spatial lags, therefore more suitable to
 257 capture highly nonlinear and localized orographic precipitation (McBratney and Webster, 1986):

$$258 \quad \gamma(h) = C_0 + (C - C_0) \left(\frac{3h}{2d} - \frac{1}{2} \left(\frac{h}{d} \right)^3 \right) \quad \text{if } 0 \leq h \leq d \quad (9.1)$$

$$259 \quad = C \quad \text{if } h > d \quad (9.2)$$

$$260 \quad \gamma_{0i} = \frac{1}{N_A} \sum_{k=1}^{N_A} \gamma_{ki} \quad (9.3)$$

$$261 \quad \gamma_{00} = \frac{1}{N_A} \sum_{k=1}^{N_A} \sum_{l=1}^{N_A} \gamma_{kl} \quad (9.4)$$

262 where h is the lag, d is the range, C and C_0 are the sill and nugget values of the semi-variogram
 263 model, N_A is the number of raingauges. The nugget is assumed to be zero if local variability and
 264 measurement error are neglected at the point scales (Diggle and Ribeiro, 2007). The interpolated
 265 rainfall difference at a location x_0 $Z_{ok}^*(x_0)$ is calculated using a weighted combination of all
 266 available differences multiplied by Kriging weights:

$$267 \quad Z_{ok}^*(x_0) = \sum_{i=1}^n \lambda_i^{ok} G(x_i) \quad (10.1)$$



$$\sum_{i=1}^n \lambda_i^{ok} = 1 \quad (10.2)$$

Optimal Kriging weights can be obtained by a series of linear equations using the Lagrange multiplier μ method:

$$\begin{pmatrix} \gamma_{11} & \cdots & \gamma_{n1} & 1 \\ \vdots & \ddots & \vdots & \vdots \\ \gamma_{1n} & \cdots & \gamma_{nn} & 1 \\ 1 & \cdots & 1 & 0 \end{pmatrix} \begin{pmatrix} \lambda_1^{OK} \\ \vdots \\ \lambda_n^{OK} \\ \mu \end{pmatrix} = \begin{pmatrix} \gamma_{01} \\ \vdots \\ \gamma_{0n} \\ 1 \end{pmatrix} \quad (11)$$

In this work, Ordinary Kriging interpolates differences between radar data and raingauge observations to produce gauge-corrected STIV_{DBKC} dataset.

2.3.5 Precipitation Assessment Metrics

Assessment metrics include the following: bias and root mean square error between radar estimation and raingauge measurement, false alarm rate, the probability of detection, threat score and Heidlke skill score, following McBride and Ebert, 2000. An instance when both radar QPE and rain gauge observation exceed a specified rain rate threshold is a hit (H); when observation matches the criterion and radar QPE does not, it is classified as a miss (M); if the opposite happens, then it is a false alarm (FA). The calculation of these metrics relied on a collection of Hs, Ms, and FAs:

$$Bias = \frac{1}{N} \sum_{n=1}^N (O_n - R_n) \quad (12)$$

$$RMSE = \sqrt{\frac{1}{N} \sum_{n=1}^N (O_n - R_n)^2} \quad (13)$$

$$FR = \frac{FA}{H+FA}, 0 \leq FR \leq 1 \quad (14)$$



$$PD = \frac{H}{H+M}, 0 \leq PD \leq 1 \quad (15)$$

$$TS = \frac{H}{H+FA+M}, 0 \leq TS \leq 1 \quad (16)$$

$$HSS = 2 * \frac{Z*H-FA*M}{((H+FA)*(Z+FA))+((M+H)*(M+Z))}, -1 \leq HSS \leq 1 \quad (17)$$

where O is the rain gauge observation, R is the radar QPE, and N is the number of points. Z represent the number of zeros, meaning both raingauge and radar do not register a rainfall record above a predefined threshold. A threat score (TS) of 0.5 means over 50% of cases meet the criterion, and the higher the better. An HSS of 0 means a forecast has the same performance as a random guess.

2.3.6 Inverse Hydrologic Correction

At flash flood timescales in headwater basins, streamflow uncertainty and precipitation uncertainty are strongly connected in a nonlinear way through rainfall runoff processes. Liao and Barros (2022) developed a Lagrangian-based framework named Inverse Rainfall Correction (IRC), allowing backpropagating streamflow uncertainty to precipitation inputs in space and time through an uncalibrated distributed hydrological model (i.e., DCHM), achieving water budget closure at the event scale in small headwater basins. As stated earlier, the uncertainties associated with parameters and the hydrological model DCHM are neglected since the model configurations have been used and improved over the past two decades for this region accounting for various soil, vegetation, and river processes (e.g., Tao and Barros, 2013, 2014, 2018 and 2019; Yildiz and Barros, 2005 and 2007; Lowman and Barros, 2016), and the IRC framework has been tested in



multiple headwater basins extensively in this region with consistent success. The detailed description of the IRC is provided in Section 2.3.8 and Appendix A.

It is worth noting that IRC is a general framework to improve QPE at the watershed scale that can be incorporated into any distributed hydrological models. Liao and Barros (2025a, 2025b) investigated the impact of model structure uncertainty and initial condition uncertainty on IRC and then the downstream product: the resulting IRC-improved QPE. The results suggest with improved watershed physics at finer resolution (e.g., river bank storage, Liao and Barros, 2025a), river routing algorithms (e.g., XY routing, Liao and Barros, 2025a) and improved antecedent soil moisture distributions (Liao and Barros, 2025b), post-IRC QPE demonstrate realistic precipitation features at high resolution that are aligned with basin topography with ridges associated with higher precipitation than valleys in general, showing a significant improvement from the original StageIV dataset which is characterized by unnatural boxy precipitation patterns in complex terrain due to resolution issues and over or underestimation depending on topography and distance from the radar site.

As briefly mentioned before, LB22 reviewed various sources of uncertainty that can prevent post-IRC QPE from achieving water budget closure, among which initial condition uncertainty in soil moisture is a noteworthy source. Improved initial condition estimation results in significantly improved post-IRC precipitation features in complex terrain by better capturing transient travel time distributions (Liao and Barros, 2025b). They found that the uncertainty tied to initial conditions is more significant for less extreme events. Nevertheless, the initial condition correction method is coupled with the IRC framework, and the complete framework is named the IRC-ICC framework. The specifics regarding the IRC, ICC, and IRC-ICC are schematically drawn in Figure 3.



329

330 <Figure 3 here please>

331

332 Using the definitions of characteristic timings shown in panels c) and d), characteristic flow
 333 regime windows are identified. In principle, the number and the size of the windows depend on
 334 the complexity of the hydrograph. ICC is only applied to windows 2 and 5 in this example, which
 335 represents a segment of the hydrograph characterized by the differences between rising points in
 336 observations and simulations, and a segment characterized by slow recession, respectively. The
 337 assumption is that precipitation uncertainty regulates streamflow differences during peak flows
 338 (i.e. windows 3 and 4). W_{nm} represents the framework state after window m for iteration n . The
 339 resolution settings for the DCHM are: spatial resolution: 250m, and temporal resolution: 5 minutes.

340 **2.3.7 Implementation of Lagrangian Tracking**

341 A flood event is simulated by the DCHM at the basin outlet with grid-based time-varying
 342 velocity fields for different soil layers. When the precipitation starts (i.e. basin-averaged
 343 precipitation $> 0.1\text{mm/hr}$), new particles (passive tracers) are launched at the same frequency of
 344 model temporal resolution (5 minutes), but only at non-zero precipitation grids in all soil layers
 345 following the velocity fields calculated by the DCHM, and the tracking resolution is 10 seconds,
 346 amounting to a release of approximately 600,000 particles for basin with an area of 120km^2 over
 347 a 24-hour period. During the tracking phase, each particle is saved along with information
 348 regarding its source location (grid-point where it originates), time of release t_i , and travel time tT
 349 (tT is defined as the difference between current time t and the time of release t_i , i.e., $tT = t - t_i$).
 350 Multiple particles from different source locations can have the same travel time, which is the basis



for identifying the number of trajectories contributing to the hydrograph at the outlet as a function of time.

2.3.8 QPE Correction Using IRC

At time t , the water difference $wd(t)$ between the observed and simulated streamflow over the time Δt between two consecutive discharge observations represents the fraction of runoff that eventually leaves the basin as streamflow. Errors in precipitation forcing propagate to the runoff, under the assumption of negligible model and parameter uncertainties, $wd(t)$ can be entirely attributed to precipitation error, which is the focus of this work.

$$wd(t) = [Q_{obs}(t) - Q_{simu}(t)] \times \Delta t \quad (18)$$

The subscripts *obs* and *simu* refer to observed and simulated discharge, respectively. The strategy for the inverse rainfall correction (IRC) using hydrograph analysis is to follow the trajectories available from the Lagrangian tracking backward from the basin outlet to the source locations at time t_i and apply a correction at the source locations proportional to the original QPE magnitude to reduce wd at time t . Detailed formulas with a conceptual drawing can be found in Appendix A. The embedded assumption is that larger QPE values have larger uncertainties. Note that QPE corrections that happened earlier in time will have an impact on runoff simulation at future times, and this is the reason why the IRC framework is a recursive framework. The detailed rainfall correction steps can be found in (Liao and Barros, 2022).



371 **2.3.9 Methods for Reducing Uncertainties from Other Sources**

372 As briefly mentioned before, uncertainties from other sources (e.g., model physics, model
373 numerical formulation, antecedent soil moisture conditions, etc.) impact travel time distributions
374 and simulated streamflow to a higher or lesser degree depending on location, antecedent
375 conditions, and storm system. Previous studies demonstrate that, for flood-producing events in
376 small headwater basins, streamflow response is largely controlled by precipitation inputs (e.g.,
377 Iwasaki et al., 2020). In this section, we briefly describe the methods used to minimize the impacts
378 from other sources to enhance water budget closure using the IRC approach.

379 As discussed in the Introduction DCHM has been used in the Appalachian Mountains at
380 event-scale (e.g., Tao and Barros, 2013, 2014, 2018 and 2019; Tao et al. 2016) and at seasonal and
381 interannual scales (Yildiz and Barros 2005, 2007 and 2009), and thus extensive analysis of
382 parameter uncertainty and model structure uncertainty has been conducted previously. Recent
383 improvements to the flood routing algorithm have resulted in significant improvements in flood
384 peak timing in headwater basins to reconcile the hydraulics of flood wave propagation on steep
385 slopes at the highest elevations with milder slopes at intermediate elevations in the valleys (Liao
386 and Barros, 2025a). Their results also suggest meandering effects, riverbank storage, and initial
387 soil moisture distributions can impact the early rising period of the hydrographs. Significant and
388 consistent improvements are made when introducing an initial condition correction (ICC) module
389 to reduce initial condition uncertainty (Liao and Barros, 2025b). This innovative ICC module is
390 coupled with the IRC framework. The red arrows in Figure 3e indicate where ICC is executed in
391 the general architecture of the IRC framework, and the specifics of the ICC module are described
392 below.



393 Particles launched during the IRC process that reached the outlet at time t are traced back
 394 directly to the IC timing or time 0, and their locations at the IC timing are shown in the bottom
 395 maps in Figure 3d (referring to control points of time t). The downstream area of the control points
 396 has shorter transportation time to arrive at the outlet (e.g., water difference ΔS_1), and the upstream
 397 area of the control points takes longer to get to the basin outlet (e.g., water difference ΔS_2).
 398 Similarly, soil moisture in the impacted area can greatly impact the size of ΔS_2 and flow conditions
 399 after the timing t_2 . Assuming initial conditions are only impactful during the early period and late
 400 recession of the hydrograph, which is supported by the fact that these events are flood-producing
 401 events with large QPE uncertainties dominating the vicinity of peak flow, ICC is used for
 402 hydrological windows outside the peak flow windows. Following the same notation (backward-
 403 in-time) in the IRC framework (Eq. 18), $wd(t)$ is calculated as the flow volume difference
 404 between observed and simulated streamflows for the time interval defined by t and $t - \Delta t$. A
 405 ‘band’ of region can therefore be identified, that is, a region formed by control points of time t
 406 and control points of time $t - \Delta t$. This ‘band’ is then referred to as the impacted area of initial soil
 407 moisture for time t , meaning basin discharge between time $t - \Delta t$ and time t is impacted by initial
 408 soil moisture at the delineated impacted area. Finally, $wd(t)$ is then converted to soil moisture
 409 content and added to initial soil moisture within the impacted area (i.e. the ‘band’) and the details
 410 can be found in Liao and Barros (2025b).

411

412 **2.3.10 Hydrological Skill Metrics**

413 The Kling-Gupta Efficiency (KGE) is calculated using observed and simulated streamflow
 414 statistics at observation resolution τ (here 15 minutes) in this work:



$$KGE_{\tau} = 1 - \sqrt{(r - 1)^2 + \left(\frac{\sigma_{sim}}{\sigma_{obs}} - 1\right)^2 + \left(\frac{\mu_{sim}}{\mu_{obs}} - 1\right)^2} \quad (19)$$

where r is the correlation between simulations and observations, σ_{obs} is the standard deviation of observed discharge, σ_{sim} is the simulated discharge standard deviation, μ_{sim} and μ_{obs} represent the average simulated and observed streamflow values, respectively.

The relative volume error (EV) is the relative difference between simulated flood volume and observed flood volume:

$$EV = \frac{V_{sim} - V_{obs}}{V_{obs}} \quad (20)$$

Where V stands for volume of the flood. An $EV > 0$, and an $EV < 0$ mean overestimation and underestimation, respectively.

EPT refers to the error in peak flow timing between observations and simulations. For its calculation, only the highest peak is selected for calculating EPT if more than one peak is present. In this work, EPT is determined by considering the entire flood rising limb to account for the steepness of the rising limb, specifically, both the flood starting timing and the maximum flood timing from the flood front rising limb are used for calculating the EPT.

EPV or error in peak volume (Q_{max} , cubic meters per second) is a relative error calculated using peak flows from observations and simulations, and the equation is below:

$$EPV = \frac{Q_{max_{sim}} - Q_{max_{obs}}}{Q_{max_{obs}}} \quad (21)$$



2.3.11 Study Domain and Model Setup

Twenty-eight headwater basins are selected in the Appalachians as illustrated in Figure 1, with basin drainage area ranging from 50 km² to 500 km². It is demonstrated in Figure 4 that these basins scatter across the entire Appalachians. For example, Basin01 and Basin30 are over 2,000 km apart, with diverse weather and climate regimes, and large differences in geomorphology and hydrogeology.

<Figure 4 here please>

Soil-related parameters are downloaded from a global high-resolution (1 km) soil data repository (Zhang et al., 2018). For each basin, the vertical hydraulic conductivity remains the same for the entire soil column. The lateral hydraulic conductivity in the unsaturated zone was assumed to be two to three orders of magnitude larger than the vertical conductivity in the shallow soil layers, with higher values where the stone fraction in the soils is higher (Carlson, 2010; Freeze and Cherry, 1979). The final scaling factors were obtained through simple sensitivity analysis to match the curvature and slope of the observed subsurface runoff recession curves (e.g., Linsley et al., 1982; Chen and Kumar, 2001; Yildiz and Barros, 2007), and scaling factors are finally determined as: 1500, 150, 15 and 1.5 for layer 1 (0-10 cm below terrain surface), layer 2 (10-75 cm below terrain surface), layer 3 (75-200 cm below terrain surface) and layer 4 (2-20 m below terrain surface), respectively. No parameter optimization is done in this work, as the primary focus of this work is to develop a QPE dataset that can consistently close the water budget while



454 controlling uncertainties from other sources, largely advancing the understanding of QPE
455 uncertainties across climate, weather, and geomorphological regimes.

456 Flood-producing events have been selected for the 28 headwater basins for recent years
457 from January 2021 to April 2024. A qualified event is determined based on the observed peak
458 flow, which must surpass 95% of available flow measurements for each basin. The choice of 95%
459 is a compromise because 99% would yield too few events, while 90% would be too close to the
460 annual flood. Additionally, rainfall runoff response time must be shorter than or equal to 6 hours
461 to be qualified as a flash flood event. Only warm season precipitation events from 2021 to 2024
462 are finally considered. Here, the warm season is specifically defined as from April 1st to September
463 30th. Note: data quality control is enforced, and events with missing streamflow records are
464 discarded.

465 For the Cataloochee Creek Basin (Basin05), located in the SAM known to have
466 experienced multiple flash floods in the past (Tao and Barros, 2013 and 2014), Liao and Barros
467 (2023) created a Historical Flood Record database (HFR) that includes a large number of extreme
468 rainfall events from 2008 to 2017. The event selection criteria when developing HFR also use the
469 same 95% flow threshold method. The difference is that the HFR also includes multiple winter-
470 time liquid precipitation events that result in cold-season flash floods. In total, there are 54 warm-
471 season events for Basin 05 in HFR, and these events are also used to expand the study sample size
472 in this work.

473 To warm up the DCHM, a traditional spin-up approach is used with iterative runs for the
474 hydrological year of 2021 (from the end of April to the end of September), and it generally reaches
475 equilibrium after 3-5 iterations. Subsequently, DCHM is continuously running from the beginning
476 of October 2021 onwards, to derive initial conditions for events after September 30th, 2021.



477 During this spin-up process, no parameter calibration is involved. The initial conditions are
478 extracted from the last iteration of spin up run, and the following model outputs generated after
479 October 1st, 2021.

480 **2.4 Caveats**

481 In the entire study domain, rain gauges are only installed in the Southern Appalachians,
482 specifically in the vicinity of the Cataloochee Creek Basin (Basin 05). However, the rest of the
483 regions are not equipped by raingauge networks, and therefore, no rain gauge bias correction is
484 done for those basins, and the downscaled original dataset StageIV (i.e., STIV_D) is used as input
485 for the IRC method and hydrological simulations in this study.

486 As an important component of the IRC framework, the Lagrangian tracking algorithm is
487 only implemented when hydrological window changes, rather than following model temporal
488 resolution (i.e., 5 minutes), due to practical computational constraints. Additionally, we do not
489 differentiate peak flow points and recession inflection points between simulations and observations
490 when classifying hydrological flow regimes/windows, and consistently use observations delineate
491 hydrological windows simply because 1) particle locations are inherently much more uncertain
492 when simulation time is getting longer partially due to numerical truncation errors and grid-based
493 abruptly-changing velocity fields used in the Lagrangian tracking algorithm, and 2) the
494 computational costs of the tracking algorithm. Very short travel times (i.e., <15 minutes) are
495 ignored because of temporal resolution restrictions from streamflow observations. A systematic
496 use of 24 hours for event total duration is imposed in this work to reduce excessive tracking
497 workload, which might be problematic for events with very long and heavy tails, though not
498 common for flash flood events in headwater basins.



499 The IRC-ICC recursive framework allows us to quantify QPE uncertainties more
 500 realistically by improving initial soil moisture estimation, and this framework is numerically
 501 efficient in terms of reaching hydrological equilibrium state within 3-5 iterations. In this work, the
 502 stable state of IRC-ICC is reached when the KGE changes are bound by 0.05.

503 3. Results and Discussion

504 3.1 Rain gauge Bias Correction

505 The climatologically corrected $STIV_{DBKC}$ fields have a significantly accurate diurnal cycle
 506 compared to only event-scale bias-corrected $STIV_{DBK}$. This process is illustrated in Figure 5 for
 507 one rain gauge from each side of the ridges (eastern side: left panel; western side: right panel) in
 508 the Southern Appalachians.

509

510 <Figure 5 here please>

511

512 Original $StageIV_D$ show higher biases over the western ridges (e.g., right panel) for all hours of
 513 day, illustrating the difficulties of capturing seeder-feeder enhancement of low-level precipitation
 514 systems (Duan and Barros, 2017). Also, the mid-day dry bias has been a problem for radar
 515 measurements in this region. (e.g., Barros and Arulraj, 2019). Results show that $StageIV_{DBKC}$
 516 datasets capture precipitation climatology better with smaller missing detection errors compared
 517 to original StageIV. Figure 6 shows the diurnal characteristics of the missing percipitaaion for
 518 two raingauge locations for winter season (January-February and March – JFM) using StageIV,
 519 and this phenonemon is observed for both the $StageIV_D$ (black) and $StageIV_{DBK}$ (cyan). These
 520 missing cases correspond to light rainfall that have small rainfall measurements at rain gauge



locations (< 1.5 mm/hr, bottom row). After applying precipitation climatology corrections, the missing issue in $\text{StageIV}_{\text{DBK}}$ is significantly alleviated and much better results are shown in $\text{StageIV}_{\text{DBKC}}$ fields (green).

<Figure 6 here please>

The seasonal HSS, TS, and RMSE of $\text{STIV}_{\text{DBKC}}$ are significantly better than those of STIV_{D} throughout the day using 10-year averages (Figure 7a). It is worth noting with increasing precipitation rate threshold (Figure 7b), threat score does not show decreasing trend, meaning raingauge bias correction for heavy rainfall events works well. Figure 7c shows RMSE performance conditional on rain rate at diurnal and seasonal scales. Overall, the RMSE is generally less than 0.1 mm/hr except in the cold-season morning and late afternoon, which can be partially attributed to snow events because these raingauges are not heated.

<Figure 7 here please>

3.2 Hydrologic Correction

The coupled IRC-ICC was originally developed and applied in Basin 05, the Cataloochee Creek Basin, and an example showing the results from iterations is demonstrated in Figure 8. The notation follows the definition in Figure 3. Note that the $\text{STIV}_{\text{DBKC}}$ data derived in Section 3.1 are



541 further downscaled to 250m and used for hydrological simulations in this section. For all other
542 basins (except Basin05), rain gauges are not available, and STIV_D data are used instead.

543

544 <Figure 8 here please>

545

546 It is demonstrated that IRC-ICC produces stable results after about 3 to 4 iterations without
547 significant oscillations for this specific extreme flood event. In general, for less significant events,
548 IRC-ICC reaches equilibrium faster (merely three iterations), providing fast and convergent
549 corrections. As explained earlier, the equilibrium state is reached and thus IRC-ICC is stopped
550 when oscillations in simulated KGE are within 0.05, and then IRC-ICC is stopped immediately.
551 This study suggests that for most events, three iterations is a good rule of thumb. The difference
552 between the initial 4D (x, y, z, t) rainfall forcing and the final result of the IRC-ICC is the general
553 IRC correction.

554

555 **3.2.1 Systematic Application of IRC-ICC**

556 The IRC-ICC is systematically executed in the 28 basins located in the Appalachians for
557 225 events, and examples are displayed in Figure 9.

558

559 <Figure 9 here please>

560



561 Simulated streamflows generally have better performances in the Northern and Southern
562 Appalachian Mountains (NAM, SAM) compared to the Central (CAM). Specifically, in the Karst
563 region along the interstate border of Virginia and West Virginia in the CAM, for Basins 13 and
564 14, where there are numerous caverns and natural tunnels facilitating fast subsurface flow response,
565 that is, sinking and subterranean streams ([https://www.dcr.virginia.gov/natural-](https://www.dcr.virginia.gov/natural-heritage/vacavetrail)
566 [heritage/vacavetrail](https://www.dcr.virginia.gov/natural-heritage/vacavetrail) and [https://docslib.org/doc/2284608/west-virginia-tax-districts-containing-](https://docslib.org/doc/2284608/west-virginia-tax-districts-containing-karst-terrain)
567 [karst-terrain](https://docslib.org/doc/2284608/west-virginia-tax-districts-containing-karst-terrain)). The current version of the DCHM does not have a specific module designed for
568 karst geology and karst hydrological processes. Thus, the IRC-ICC results in these locations are
569 impacted by model structural uncertainty. Here, the advantage of not calibrating model parameters
570 becomes apparent. It would be possible to calibrate model parameters to improve model
571 simulations; however, the physical basis and transferability of the IRC-ICC results would be
572 compromised. The 10 events in Basins 13 and 14 are therefore discarded (example: Figure A3).
573 This point of discussion is highlighted here to reinforce the value of the data set presented in this
574 manuscript for applications with other hydrologic models, including model calibration, where
575 model structural uncertainty is not a primary concern at resolved scales.

576 Event 2021-06-10 in Basin 19 (see Figure A3) is an example of an event with a complex
577 hydrograph (e.g., multiple minor flood peaks around one major flood peak) that requires more
578 hydrological windows (see Figure 3). Subtle changes in the hydrograph shape could be indicative
579 of spatial shifts in runoff production from one tributary to another following the track of storm
580 cells over the basin. Indeed, depending on the weather system and regional topography, the travel
581 velocity of such cells and their life-cycle may require finer spatial and temporal resolution both
582 for the hydrological model and for the tracking algorithm to capture changes in the spatial structure
583 of precipitation, especially in the case of summer thunderstorms. For the systematic production of



584 this data set, a 5-window IRC-ICC framework was applied, including a pre-rising-point segment,
585 rising limb, early recession, and late recession (separated by the recession inflection point).

586

587 **3.2.2 IRC and IRC-ICC Precipitation Corrections**

588 Accumulated rainfall totals per rainfall event are calculated for both the IRC-only product
589 and post IRC-ICC products. Subsequently, these rainfall totals are directly compared against
590 original product $STIV_{DBKC}$. Examples are shown in Figure 10, categorized by seasons in the
591 Cataloochee Creek Basin (Basin05). Again, the warm season is defined as April 1st to September
592 30th, and the remaining events are defined as the cold season, with only liquid precipitation events
593 studied in this work.

594

595 <Figure 10 here please>

596

597 The original QPE (**a1** and **b1**) shows abrupt changes in rainfall intensity, which is a
598 common issue of radar observations at high spatial resolution. On the contrary, the IRC-corrected
599 precipitation maps demonstrate precipitation features aligning with landform, showing strong
600 spatial precipitation gradients along ridges and adjacent valleys (examples are listed in Figure A2).
601 The spatial correlation between orographic precipitation and topography is observed across all
602 mountain ranges, including the Appalachians (e.g., Konrad II, 1994; Smith et al., 2011; Wolvin et
603 al., 2024). Note the dark blue colors in Figure 10 corresponding to very low precipitation near the
604 basin outlet are an artifact of the IRC tied to very short travel times that cannot be fully resolved
605 even at fine scales of 250m and 5minutes. However, these artifacts are much reduced for the IRC-



ICC due to the reduction of uncertainty in initial conditions, as shown for the 2009-10-14, 2009-04-20, and 2013-04-12 events because of overall basin-wide travel time improvement. It is worth noting that these three events are relatively mild events, indicating a larger impact of IC on relatively less extreme events because of the critical role of IC in runoff generation mechanisms and travel times distributions. Thus, the extreme event precipitation product obtained from IRC-ICC is the data set recommended for applications with other hydrologic models.

612

613 3.2.3 Precipitation and Hydrologic Statistics

Event-total precipitation maps are calculated for each basin and event, and basin-scale precipitation statistics (e.g., mean and standard deviation) are derived for each event-total precipitation map. These statistics are plotted in Figure 11, and subregions are separated by vertical black lines. Basins 01 to 11 are located in the SAM, Basins 12 to 20 are located in the CAM, and Basins 21 to 30 are located in the NAM. Basins 13 and 14 are not included in the statistics.

619 <Figure 11 here please>

It is clearly demonstrated that the change in the mean (i.e., basin-averaged event total QPE) is relatively small (from 36.10mm to 38.07mm) compared to the change in the standard deviation (from 6.63mm to 14.08mm) after the application of IRC-ICC. The small standard deviation of the original QPE suggests that the original QPE data are spatially tightly clustered with low variability (see Figure 10a for boxy rainfall features), while the larger standard deviation post-IRC-ICC indicates spatial variability is enhanced, which is highlighted by the terrain-aligned precipitation features in Figure 10c. The relatively small change in the mean indicates that the original input precipitation (i.e., StageIV_{DBKC} for Basin 05, and StageIV_D for the remaining basins) does not



628 contain significant unconditional systematic biases across basins and events, which would lead to
 629 consistent positive or negative flood volume errors. As an exception, it is worth noting that the
 630 standard deviation of Basin 05 events does not change significantly after the IRC-ICC compared
 631 to other basins and events because rain gauge corrections from the IPHEX network are employed
 632 in Basin 05 but not anywhere else. It can never be overly emphasized that even after rain gauge
 633 bias correction, essentially a point-scale correction method, the resulting flood hydrograph exhibits
 634 significant water budget closure errors (see Figure 12 for more discussion) on account of the high
 635 heterogeneous nature of QPE in complex terrain.

636 The hydrologic statistics described in Table 1 using all studied events are plotted in Figure
 637 12.

638 <Figure 12 here please>

639 Figure 12 shows that the median KGE across events is improved from 0.36, 0.39, 0.27 to
 640 0.89, 0.74, 0.84 for SAM, CAM, and NAM, respectively. It should be pointed out that QPE
 641 changes for Basin 05 events (event numbers 55 to 108) are important for improving water budget
 642 closure, albeit small in magnitude compared to other events in other basins, as shown in Figure 11
 643 and 12, and yet critical to capture the complex precipitation heterogeneity in complex terrain to
 644 close the water budget. The results for Basin 05 illustrate the limitations of rain gauge-based bias
 645 corrections in complex terrain in general. The relatively small improvement shown in the CAM is
 646 partially attributed to the fact that DCHM does not have a proper representation of subterranean
 647 rivers in karst terrain, causing large baseflow errors during hydrograph recession and thus low
 648 KGE values. Nevertheless, for flash flood applications, peak flow magnitude, flood flow timing,
 649 and event flow volume are the most important forecast objectives, corresponding to the 2nd, 3rd,
 650 and 4th horizontal panels in Figure 12. Overall, flood volume error (EV) is controlled within $\pm 10\%$



651 for over 90% of the studied events (the 2nd panel), with the median EV error being less than 5% in
652 the SAM and NAM after IRC-ICC corrections. Flood peak volume (the 3rd panel) is generally
653 controlled within 20%, which is very good for extreme events in regions without ground-based
654 observations except for radars placed far away. This is demonstrated by Tropical Storm Fred on
655 2021-08-17: an event that caused floods in multiple SAM basins, caused five deaths, and resulted
656 in an economic loss of more than 1 billion dollars. Note the KGE for this event is improved to 0.9,
657 and peak timing errors are <30 minutes using IRC-ICC. Timing errors (shown in the 4th subplot)
658 are bounded by ± 60 minutes for the major of the events for post IRC-ICC datasets, though some
659 outliers exist potentially due to complex antecedent land surface physics (e.g., rain on snow) for
660 April events, particularly in the CAM and NAM.

661 Events associated with significant timing errors (more than ± 90 minutes) are investigated
662 in detail. These include the 2023-07-08 event (event number 185) for Basin 27, which is located
663 in New Hampshire (the estimated flood front occurs too early by 2.5 hours). This was a localized
664 summer thunderstorm event, only taking 30 minutes to reach its peak flow. The fast changes in the
665 hydrological regime require much more windows than the current classic 5-window settings used
666 in the IRC-ICC framework. The event on 2022-05-27 (event number 118) in Basin16 located in
667 West Virginia is characterized by a slow rising limb. Note Basin16 is partially located in a complex
668 region with karst features (e.g., sink holes) in the Greenbrier-river valley. Finally, the event 2021-
669 09-22, a complex rainfall system characterized by multiple rain cells passing through the Basin 19
670 quickly (event number 133), requiring smaller hydrological windows to capture highly variable
671 rainfall-runoff responses than the 5-window default IRC-ICC architecture: baseflow segment, pre-
672 rising segment, flood rising limb, early and late recession.



Overall, large improvements in QPE are achieved, resulting in hydrological improvements in aspects of peak magnitude, flood total volume and flood front timing. Due to the dependence of IRC-ICC on travel time distributions, it cannot be used when precipitation is missing or there are severe timing errors because of the lack of water travel time trajectories to distribute corrections. From a practical point of view, the QPE IRC-ICC correction is in nature a type of space-time bias correction. The improved QPE data facilitates the development of QPE error models, which is demonstrated by the same authors (e.g., Liao and Barros, 2023), providing a path towards correcting remote-sensing products to support hydrometeorological studies and advancing the calibration of hydrological models with significantly less forcing uncertainty.

3.2.4 Independent Verification

As mentioned in the introduction, precipitation measurements are limited in the Appalachians except for the IPHEX rain gauge network (Figure 1). Currently, the NEXRAD radar network remains the widely used precipitation monitoring system in this region in spite of well-documented low radar quality coverage over radar gaps in the mountains. The Multi-Radar/Multi-Sensor (MRMS) product (Zhang et al., 2016), which is developed using NEXRAD radar measurements similar to StageIV, is created at 1km resolution and is used here for independent verification.

First, original MRMS data are downscaled to the same resolution as StageIV_D datasets (250m, 5min) and used as inputs for DCHM. Hydrological simulations in this section are using the same model configuration and initial model states for the purpose of a meaningful comparison, including the following datasets: MRMS_D, StageIV_D, and IRC-ICC StageIV_D as shown in Figure 13. Figure 13a shows that MRMS and StageIV QPE have similar results. Second, the IRC-ICC StageIV_D



695 have generally a good agreement with $MRMS_D$ similar to $StageIV_D$. However, for some cases,
696 where rainfall is dramatically underestimated by the radar system and KGE values are low, IRC-
697 ICC is shown to provide effective corrections. Otherwise, the IRC-ICC generates physically
698 constrained corrections spatially (see Figure 10), achieving high KGE values for flood simulations.
699 Figure 13b shows the histogram of the KGE values across different rainfall products for all events.
700 Overall, simulated streamflows using $MRMS_D$ and $StageIV_D$ exhibit similar hydrologic
701 performance (the median KGE across events is close to 0.20), on the contrary, post-IRC-ICC
702 $StageIV_D$ produce flood simulations with a median KGE above 0.80.

703

704 **4. Discussion and Future Work**

705 Limitations in this study stem mainly from computational constraints rather than
706 methodology. A default 24-hour flood duration window is imposed, implying that for long-lasting
707 floods, due to significant slow interflow and baseflow contributions, are not considered. The
708 current version of the IRC-ICC framework was built to support flash flood studies and only targets
709 shallow subsurface moisture transport, given the critical importance of shallow soil moisture on
710 the regulation of flood generation and propagation in steep terrain. It is worth noting that for long-
711 lasting rainfall events or regions with relatively flat terrain, slow interflows would become more
712 important in terms of regulating flood timing, flood volume, and post IRC-ICC QPE.

713 While the IRC results could be further optimized if carried out at the same frequency as
714 the model resolution, therefore eliminating any artifacts due to inadequate sampling and updating
715 of travel time distributions, and while there is room to improve the IRC-ICC framework through
716 improved model physics and resolution, utilizing 3D velocity fields to capture the full travel time



distributions, and using different models to generate IRC ensembles. to test and calibrate hydrologic models for an intercomparison study, advancing flood forecasting skill, and to support emergency management response.

720

5. Data Availability Statement

The StageIV-IRC dataset at 250 m 5-minute resolution for 26 basins and 215 events is available at: <https://doi.org/10.5281/zenodo.14028866>. (Liao and Barros, 2025c), excluding Basin 13 and 14 based on previous discussion. Associated geographic documentation of the selected basins is also provided via the same link. Initial soil moisture distributions for the studied events are also available in the same Zenodo repository.

727

6. Conclusion

QPE has been an enduring challenge in hydrology, particularly in complex terrain. Ground-based radar QPE is plagued with uncertainties from multiple sources, while rain gauge networks are scarce and suffer from the lack of representativeness in the mountains. To address this grand challenge, we develop a series of corrections from point-scale to watershed-scale encompassing event bias, climatology, and water budget closure: the IRC-ICC framework. To our knowledge, this is the first QPE dataset that meets standard statistical evaluations against point-based measurements where available and meets water budget closure at flood-event scale, consistent with nonlinear rainfall-runoff processes in headwater basins, and achieves superior hydrological performance at sub-hourly.



738 The IRC-ICC framework is successfully adopted in 26 mountainous basins (excluding the
739 basins that are heavily overlapped with Karst terrain) in the Appalachians for 215 events with
740 robust success, yielding substantial improvements of streamflow simulation, particularly in terms
741 of flood volume and timing. The tracking algorithm in the IRC-ICC framework is only updated
742 when shifting from one hydrological window to another, but not every time step. With enough
743 computational resources, post-IRC-ICC QPE data should further improve by capturing transient
744 travel time distributions between model time steps.

745 When using the StageIV-IRC product, flood timing errors are controlled with one hour for
746 90% of events, compared to less than 20% when using original StageIV, while the median KGE
747 improved from 0.34 to 0.86 across the events. This change in KGE is achieved by significant
748 changes in the space-time variance of precipitation that in turn impacts the space-time variability
749 of rainfall-runoff processes. Results illustrate the importance of initial conditions for less severe
750 rainfall events, particularly during the beginning of the event, which influences subsequent
751 streamflow simulations. It should be emphasized that physical parameters are not calibrated for
752 any precipitation event in any basin in this work. This physics-based IRC-ICC framework can
753 capture the fundamental physics involved in flash flood events: essentially the fast rainfall-runoff
754 responses in surface and shallow subsurface layers; therefore, skillful hydrologic prediction is
755 achieved without model calibration. Instead, the focus is on getting the forcing right.

756 The IRC-ICC is a general framework that can be incorporated into any distributed
757 hydrological model. Thus, the StageIV-IRC dataset also enables meaningful intercomparison
758 among different radar QPE datasets, providing physics insights into QPE error structure from a
759 water budget closure perspective, toward improving radar retrievals and to characterize radar-
760 specific errors related to radar operations at high spatial resolution in the mountains. The

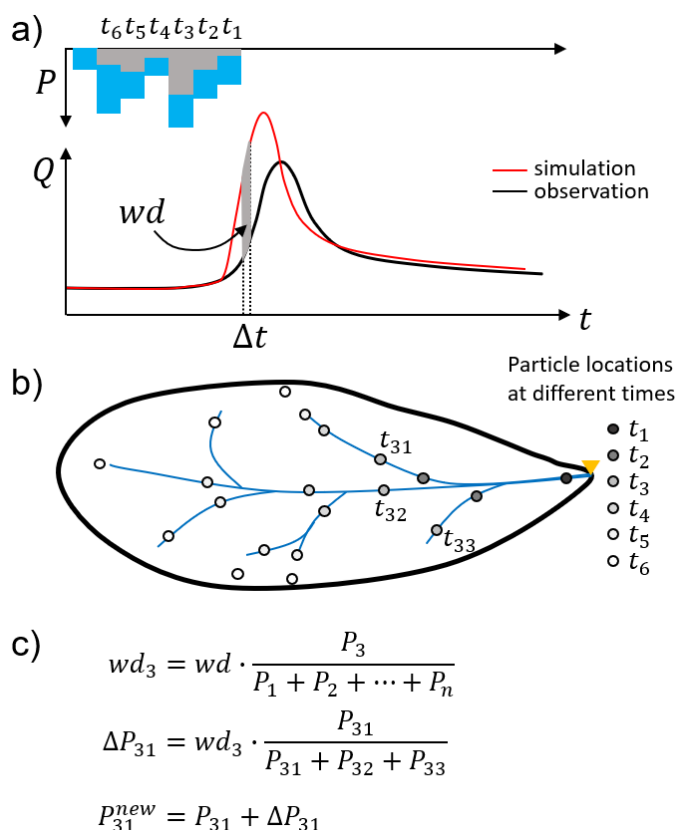


761 demonstrated success of StageIV-IRC in ungauged basins strongly supports the use of IRC-ICC
762 in mountainous regions worldwide, where rain gauges are generally not available. Further, this
763 dataset can be utilized as a reference for building machine learning models (or even deep-learning
764 models when the number of studied precipitation events is expanded) that can learn the QPE
765 uncertainties conditional on time of day, weather, climate and geomorphological regimes for both
766 radar QPE analysis and forecasts, advancing the understanding and quantification of orographic
767 precipitation uncertainty at high resolution across global mountains.

768 **7. Appendix A**

769 The detailed distribution process of water difference (wd) is illustrated in Figure A1 following
770 Section 2.3.8.

771



772

773 **Figure A1** - Schematic depiction of the IRC framework and key mathematical equations. Panel
 774 (a) illustrates the nonlinear relationship between streamflow and precipitation, where wd
 775 represents the residual between discharge simulations and observations at the basin outlet. The
 776 variation of precipitation in the basin as a function of time is shown by the basin hyetograph in
 777 blue. The hyetograph time series (blue) spans the duration of the precipitation event between t_1
 778 to t_n . In gray is the hyetograph over the area of interest for panels (b) and (c). To map the
 779 streamlines, water particles are launched every time step and their trajectory to the outlet is tracked
 780 and saved. Panel (b) shows the source areas of water particles launched at various time steps
 781 ($t_1, t_2, \dots t_6 \dots$) from all locations where runoff is produced, and the particles are tracked until they
 782 eventually reach the basin outlet. The streamlines of particles that reach the outlet at the same time



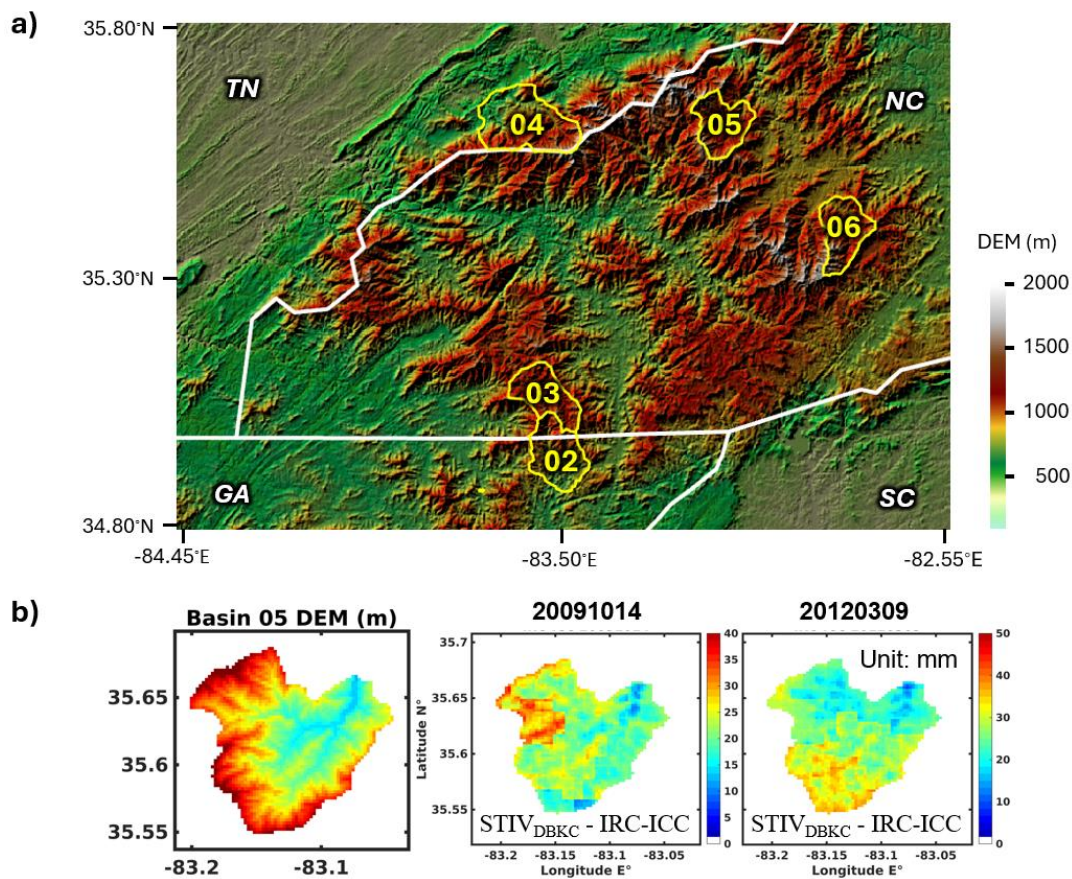
783 are used to distribute the residuals backwards to the runoff source areas where the particles were
 784 originally launched (e.g., the three particles t_{31} , t_{32} , and t_{33} that reach the basin outlet at time t_3).
 785 Panel (c) shows the algorithm to calculate the rainfall bias correction at location t_{31} due to the
 786 residual wd_3 at time t_3 . P_i is basin averaged rainfall at time t_i , and wd_3 is the runoff volume to
 787 be corrected at time step t_3 . ΔP_{31} is the precipitation correction for pixel t_{31} , and precipitation
 788 amount at pixel t_{31} before and after IRC are denoted by P_{31} and P_{31}^{new} . This figure is adapted from
 789 Liao and Barros (2025b).

790

791 A zoom in map of the Southern Appalachians is plotted associated with DEM maps of other basins.
 792 A complete set of maps for each individual basin can be requested. Note, the rain gauges used in
 793 this study are plotted in Figure 1, and they are primarily near Basin05.



794



795

796 **Figure A2** – A zoom-in map of the Figure 4 for watersheds in the Southern Appalachians (Panel
797 a). The DEM map and examples of rainfall event accumulation of Basin 05 (Panel b) to show
798 rainfall alignment with topography.

799

800

801

802

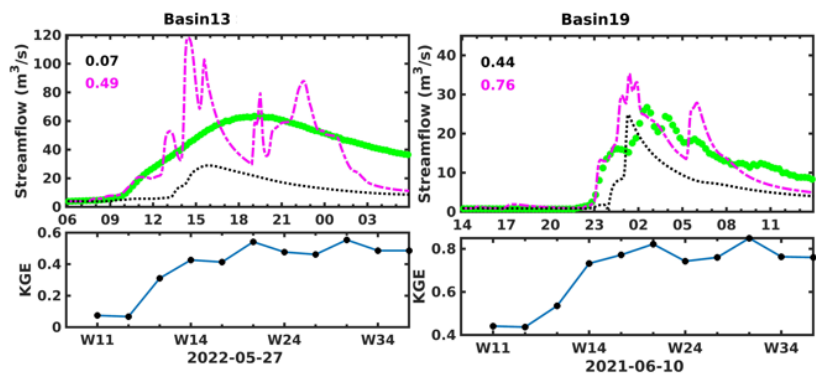


Figure A3 – Examples of the coupled IRC-ICC framework application in Basin 13 and Basin 19 for discussion in the manuscript. Basin 13 is located in Karst terrain, while the event in Basin 19 is an example with a complex hydrograph.

CREDIT AUTHOR STATEMENT

M. Liao: Methodology, Data curation, Writing - original draft, Investigation. A. P. Barros: Conceptualization, Methodology, Writing - review & editing, Supervision, Project administration, Funding acquisition.

COMPETING INTERESTS

The authors declare there are no competing interests.

ACKNOWLEDGMENTS

The work was supported by NASA Earth System Science Fellowship associated with the first author and supported by a joint effort from NASA grant 80NSSC19K0685 and a grant from the IBM Accelerator program with the second author.



819 REFERENCES

- 820 Alimonti, G., Mariani, L., Prodi, F., & Ricci, R. A. (2022). A critical assessment of extreme
 821 events trends in times of global warming. *European Physical Journal - Plus*, 137, 112.
 822 <https://doi.org/10.1140/epjp/s13360-021-02243-9>
- 823 Allen, J. T. (2018). Climate change and severe thunderstorms. In Oxford research encyclopedia
 824 of climate science. <https://doi.org/10.1093/acrefore/9780190228620.013.62>
- 825 Andrieu, H., Creutin, J. D., Delrieu, G., & Faure, D. (1997). Use of a weather radar for the
 826 hydrology of a mountainous area. Part I: Radar measurement interpretation. *Journal of*
 827 *Hydrology*, 193(1-4), 1-25.
- 828 Areerachakul, N., Prongnuch, S., Longsomboon, P., & Kandasamy, J. (2022). Quantitative
 829 precipitation estimation (QPE) rainfall from meteorology radar over Chi Basin. *Hydrology*,
 830 9(10), 178. <https://doi.org/10.3390/hydrology9100178>
- 831 Arulraj, M., & Barros, A. P. (2017). Shallow precipitation detection and classification using
 832 multifrequency radar observations and model simulations. *Journal of Atmospheric and Oceanic*
 833 *Technology*, 34(9), 1963-1983. <https://doi.org/10.1175/JTECH-D-17-0060.1>
- 834 Arulraj, M., & Barros, A. P. (2021). Automatic detection and classification of low-level
 835 orographic precipitation processes from space-borne radars using machine learning. *Remote*
 836 *Sensing of Environment*, 257, 112355. <https://doi.org/10.1016/j.rse.2021.112355>
- 837 Barros, A., & Arulraj, M. (2020). Remote sensing of orographic precipitation. In V. Levizzani,
 838 C. Kidd, D. B. Kirschbaum, C. D. Kummerow, K. Nakamura, & F. J. Turk (Eds.), *Satellite*
 839 *precipitation measurement*. Springer. https://doi.org/10.1007/978-3-030-35798-6_6
- 840 Barros, A., Miller, D., Wilson, A., Cutrell, G., Arulraj, M., Super, P., & Petersen, W. (2017).
 841 GPM Ground Validation Southern Appalachian Rain Gauge IPHEX [indicate subset used].
 842 Dataset available online from the NASA Global Hydrometeorology Resource Center DAAC,
 843 Huntsville, Alabama, U.S.A. DOI:
 844 <http://dx.doi.org/10.5067/GPMGV/IPHEX/GAUGES/DATA301>
- 845 Barros, A.P., Petersen, W., Schwaller, M., Cifelli, R., Mahoney, K., Peters-Liddard, C.,
 846 Shepherd, M., Nesbitt, S., Wolff, D., Heymsfield, G. & Starr, D. (2014) NASA GPM-Ground
 847 Validation: Integrated Precipitation and Hydrology Experiment 2014 Science Plan. EPL/Duke
 848 University: Durham, N.C. <https://doi.org/10.7924/G8CC0XMR>.
- 849 Berndt, C., Rabiei, E., & Haberlandt, U. (2014). Geostatistical merging of rain gauge and radar
 850 data for high temporal resolutions and various station density scenarios. *Journal of Hydrology*,
 851 508, 88-101. <https://doi.org/10.1016/j.jhydrol.2013.10.028>
- 852 Bindlish, R. and Barros, A.P., (1996): Aggregation of Digital Terrain Data Using a Modified
 853 Fractal Interpolation Scheme. *Computers & Geosciences*, 22, 907-917.
- 854 Bindlish, R., & Barros, A. P. (2000). Disaggregation of rainfall for one-way coupling of
 855 atmospheric and hydrological models in regions of complex terrain. *Global and Planetary*
 856 *Change*, 25(1-2), 111-132. [https://doi.org/10.1016/S0921-8181\(00\)00024-2](https://doi.org/10.1016/S0921-8181(00)00024-2)



- 858 Bohling, G. (2005). Introduction to geostatistics and variogram analysis. Kansas geological
 859 survey, 1(10), 1-20.
- 860 Borga, M., Stoffel, M., Marchi, L., Marra, F., & Jakob, M. (2014). Hydrogeomorphic response to
 861 extreme rainfall in headwater systems: Flash floods and debris flows. *Journal of Hydrology*, 518,
 862 194-205.
- 863 Buytaert, W., Celleri, R., Willems, P., De Bievre, B., & Wyseure, G. (2006). Spatial and
 864 temporal rainfall variability in mountainous areas: A case study from the south Ecuadorian
 865 Andes. *Journal of hydrology*, 329(3-4), 413-421. <https://doi.org/10.1016/j.jhydrol.2006.02.031>
- 866 Carlson, D., (2010). Influence of lithology on vertical anisotropy of permeability at a field scale
 867 for select Louisiana geologic units. *Gulf Coast Association of Geological Societies Transactions*,
 868 60: 103-118.
- 869 Cassiraga, E., Gómez-Hernández, J. J., Berenguer, M., Sempere-Torres, D., & Rodrigo-Illarri, J.
 870 (2021). Spatiotemporal precipitation estimation from rain gauges and meteorological radar using
 871 geostatistics. *Mathematical Geosciences*, 53, 499-516. [https://doi.org/10.1007/s11004-020-](https://doi.org/10.1007/s11004-020-09882-1)
 872 [09882-1](https://doi.org/10.1007/s11004-020-09882-1)
- 873 Chen, J., Kumar, P., 2001. Topographic influence on the seasonal and interannual variation of
 874 water and energy balance of basins in North America. *Journal of Climate*, 14(9).
- 875 Czigány, S., Pirkhoffer, E., & Geresdi, I. (2010). Impact of extreme rainfall and soil moisture on
 876 flash flood generation. *Quarterly Journal of the Hungarian Meteorological Service*, 114(1-2),
 877 79-100.
- 878 Deijns, A. A., Dewitte, O., Thiery, W., d'Oreye, N., Malet, J. P., & Kervyn, F. (2022). Timing
 879 landslide and flash flood events from SAR satellite: a regionally applicable methodology
 880 illustrated in African cloud-covered tropical environments. *Natural Hazards and Earth System*
 881 *Sciences*, 22(11), 3679-3700. <https://doi.org/10.5194/nhess-22-3679-2022>
- 882 Delrieu, G., Wijbrans, A., Boudevillain, B., Faure, D., Bonnifait, L., & Kirstetter, P. E. (2014).
 883 Geostatistical radar-rain gauge merging: A novel method for the quantification of rain estimation
 884 accuracy. *Advances in Water Resources*, 71, 110-124.
 885 <https://doi.org/10.1016/j.advwatres.2014.06.005>
- 886 Diggle, P. and Ribeiro, P. J., 2007. Model-based geostatistics. Springer Series in Statistics, 230.
- 887 Dinku, T., Anagnostou, E. N., & Borga, M. (2002). Improving radar-based estimation of rainfall
 888 over complex terrain. *Journal of Applied Meteorology and Climatology*, 41(12), 1163-1178.
 889 [https://doi.org/10.1175/1520-0450\(2002\)041<1163:IRBEOR>2.0.CO;2](https://doi.org/10.1175/1520-0450(2002)041<1163:IRBEOR>2.0.CO;2)
- 890 Diomede, T., Davolio, S., Marsigli, C., Miglietta, M. M., Moscatello, A., Papetti, P., ... &
 891 Malguzzi, P. (2008). Discharge prediction based on multi-model precipitation forecasts.
 892 *Meteorology and atmospheric physics*, 101, 245-265. <https://doi.org/10.1007/s00703-007-0285-0>
- 893 Dobler, C., Hagemann, S., Wilby, R. L., & Stötter, J. (2012). Quantifying different sources of
 894 uncertainty in hydrological projections in an Alpine watershed. *Hydrology and Earth System*
 895 *Sciences*, 16(11), 4343-4360. <https://doi.org/10.5194/hess-16-4343-2012>
- 896 Duan, Y., & Barros, A. P. (2017). Understanding how low-level clouds and fog modify the
 897 diurnal cycle of orographic precipitation using in situ and satellite observations. *Remote*
 898 *Sensing*, 9(9), 920. <https://doi.org/10.3390/rs9090920>



- 899 Durden, S. L., Haddad, Z. S., Kitiyakara, A., & Li, F. K. (1998). Effects of nonuniform beam
900 filling on rainfall retrieval for the TRMM precipitation radar. *Journal of Atmospheric and*
901 *Oceanic Technology*, 15(3), 635-646. [https://doi.org/10.1175/1520-](https://doi.org/10.1175/1520-0426(1998)015<0635:EONBFO>2.0.CO;2)
902 [0426\(1998\)015<0635:EONBFO>2.0.CO;2](https://doi.org/10.1175/1520-0426(1998)015<0635:EONBFO>2.0.CO;2)
- 903 Foresti, L., & Pozdnoukhov, A. (2012). Exploration of alpine orographic precipitation patterns
904 with radar image processing and clustering techniques. *Meteorological Applications*, 19(4), 407-
905 419. <https://doi.org/10.1002/met.272>
- 906 Freeze, R.A., Cherry, J.A., 1979. *Groundwater*. Englewood Cliffs, N.J. : Prentice-Hall.
- 907 Fulton, J., & Ostrowski, J. (1998). Measuring real-time streamflow using emerging technologies:
908 Radar, hydroacoustics, and the probability concept. *Journal of Hydrology*, 357(1-2), 1-10.
909 <https://doi.org/10.1016/j.jhydrol.2008.03.028>
- 910 Gentilucci, M., Bufalini, M., D'Aprile, F., Materazzi, M., & Pambianchi, G. (2021). Comparison
911 of data from rain gauges and the IMERG product to analyse precipitation in mountain areas of
912 central Italy. *ISPRS International Journal of Geo-Information*, 10(12), 795.
913 <https://doi.org/10.3390/ijgi10120795>
- 914 Goudenhoofdt, E., & Delobbe, L. (2009). Evaluation of radar-gauge merging methods for
915 quantitative precipitation estimates. *Hydrology and Earth System Sciences*, 13(2), 195-203.
916 <https://doi.org/10.5194/hess-13-195-2009>
- 917 Grillakis, M. G., Koutroulis, A. G., Komma, J., Tsanis, I. K., Wagner, W., & Blöschl, G. (2016).
918 Initial soil moisture effects on flash flood generation—A comparison between basins of
919 contrasting hydro-climatic conditions. *Journal of Hydrology*, 541, 206-217.
- 920 Gupta, H. V., Kling, H., Yilmaz, K. K., & Martinez, G. F. (2009). Decomposition of the mean
921 squared error and NSE performance criteria: Implications for improving hydrological
922 modelling. *Journal of hydrology*, 377(1-2), 80-91. <https://doi.org/10.1016/j.jhydrol.2009.08.003>
- 923 Gupta, V., Nautiyal, H., Kumar, V., Jamir, I., & Tandon, R. S. (2016). Landslide hazards around
924 Uttarkashi township, Garhwal Himalaya, after the tragic flash flood in June 2013. *Natural*
925 *Hazards*, 80, 1689-1707. <https://doi.org/10.1007/s11069-015-2048-4>
- 926 Harrison, D. L., Driscoll, S. J., & Kitchen, M. (2000). Improving precipitation estimates from
927 weather radar using quality control and correction techniques. *Meteorological Applications*, 7(2),
928 135-144. <https://doi.org/10.1017/S1350482700001468>
- 929 Huffman, G. J., R. F. Adler, D. T. Bolvin, G. J. Gu, E. J. Nelkin, K. P. Bowman, Y. Hong, E. F.
930 Stocker, and D. B. Wolff (2007), The TRMM multisatellite precipitation analysis (TMPA):
931 Quasi-global, multiyear, combined-sensor precipitation estimates at fine scales, J.
932 *Hydrometeorol.*, 8(1), 38–55. <https://doi.org/10.1175/JHM560.1>
- 933 Iwasaki, K., Katsuyama, M., & Tani, M. (2020). Factors affecting dominant peak-flow runoff-
934 generation mechanisms among five neighbouring granitic headwater catchments. *Hydrological*
935 *Processes*, 34(5), 1154-1166. <https://doi.org/10.1002/hyp.13656>
- 936 Kim, G., & Barros, A. P. (2001). Quantitative flood forecasting using multisensor data and
937 neural networks. *Journal of Hydrology*, 246(1-4), 45-62. [https://doi.org/10.1016/S0022-](https://doi.org/10.1016/S0022-1694(01)00353-5)
938 [1694\(01\)00353-5](https://doi.org/10.1016/S0022-1694(01)00353-5)



- 939 Kobold, M., & Sušelj, K. (2005). Precipitation forecasts and their uncertainty as input into
 940 hydrological models. *Hydrology and Earth System Sciences*, 9(4), 322-332.
 941 <https://doi.org/10.5194/hess-9-322-2005>
- 942 Kochendorfer, J., Rasmussen, R., Wolff, M., Baker, B., Hall, M. E., Meyers, T., ... & Leeper, R.
 943 (2017). The quantification and correction of wind-induced precipitation measurement errors.
 944 *Hydrology and Earth System Sciences*, 21(4), 1973-1989. [https://doi.org/10.5194/hess-21-1973-](https://doi.org/10.5194/hess-21-1973-2017)
 945 [2017](https://doi.org/10.5194/hess-21-1973-2017)
- 946 Komma, J., Reszler, C., Blöschl, G., & Haiden, T. (2007). Ensemble prediction of floods–
 947 catchment non-linearity and forecast probabilities. *Natural Hazards and Earth System Sciences*,
 948 7(4), 431-444.
- 949 Konrad II, C. E. (1994). Moisture trajectories associated with heavy rainfall in the Appalachian
 950 region of the United States. *Physical Geography*, 15(3), 227-248.
 951 <https://doi.org/10.1080/02723646.1994.10642514>
- 952 Kreklow, J., Tetzlaff, B., Burkhard, B., & Kuhnt, G. (2020). Radar-based precipitation
 953 climatology in Germany—developments, uncertainties and potentials. *Atmosphere*, 11(2), 217.
 954 <https://doi.org/10.3390/atmos11020217>
- 955 Laiolo, P., Gabellani, S., Campo, L., Silvestro, F., Delogu, F., Rudari, R., ... & Puca, S. (2016).
 956 Impact of different satellite soil moisture products on the predictions of a continuous distributed
 957 hydrological model. *International Journal of Applied Earth Observation and Geoinformation*,
 958 48, 131-145. <https://doi.org/10.1016/j.jag.2015.06.002>
- 959 Li, J., & Heap, A. D. 2008. A review of spatial interpolation methods for environmental
 960 scientists. 11-12.
- 961 Liao, M., & Barros, A. P. (2019). The Integrated Precipitation and Hydrology Experiment-
 962 Hydrologic Applications for the Southeast US (IPHEX-H4SE) Part IV: High-Resolution
 963 Enhanced Stage IV-Rain gauge Combined Precipitation Product [Dataset]. Durham, NC: Duke
 964 Digital Repository. <https://idn.duke.edu/ark:/87924/r4pc2zd75>
- 965 Liao, M., & Barros, A. P. (2022). Toward optimal rainfall – Hydrologic QPE correction in
 966 headwater basins. *Remote Sensing of Environment*, 279, 113107.
 967 <https://doi.org/10.1016/j.rse.2022.113107>
- 968 Liao, M., & Barros, A.P., (2025a). Model Celerity-Discharge Behavior in Complex Terrain to
 969 Improve Orographic Quantitative Precipitation Estimation and Hydrologic Prediction in
 970 Headwater Basins. *Water Resources Research*, <https://doi.org/10.1029/2024WR038446>
- 971 Liao, M., & Barros, A.P., (2025b). Toward optimal rainfall – Hydrologic QPE Correction in
 972 Headwater Basins — Closing the Water Budget within Observational Uncertainty Through
 973 Correcting Initial Soil Moisture Conditions. *J. Hydrology-Reg. Studies*,
 974 <https://doi.org/10.1016/j.ejrh.2025.102700>.
- 975 Liao, M., & Barros, A. (2025c). StageIV-IRC – A High-resolution Dataset of Extreme
 976 Orographic Quantitative Precipitation Estimates (QPE) Constrained to Water Budget Closure for
 977 Historical Floods in the Appalachian Mountains [Data set]. Zenodo.
 978 <https://doi.org/10.5281/zenodo.14028866>
- 979



- 980 Lin, Y., & Mitchell, K. E. (2005), The NCEP stage II/IV hourly precipitation analyses:
 981 Development and applications, paper presented at 19th Conference on Hydrology [Dataset], Am.
 982 Meteorol. Soc., San Diego, Calif., 9–13 Jan.
- 983 Linsley, R.K., Kohler, J., Max A., Paulhus, J.L.H., (1982). Hydrology for Engineers. Water
 984 Resources and Environmental Engineering. McGraw-Hill, New York.
- 985 Lumbroso, D., & Gaume, E. (2012). Reducing the uncertainty in indirect estimates of extreme
 986 flash flood discharges. *Journal of hydrology*, 414, 16-30.
- 987 Maggioni, V., & Massari, C. (2018). On the performance of satellite precipitation products in
 988 riverine flood modeling: A review. *Journal of hydrology*, 558, 214-224.
- 989 Marchi, L., Borga, M., Preciso, E., & Gaume, E. (2010). Characterisation of selected extreme
 990 flash floods in Europe and implications for flood risk management. *Journal of Hydrology*, 394(1-
 991 2), 118-133.
- 992 McBratney, A. B., & Webster, R. (1986). Choosing functions for semi-variograms of soil
 993 properties and fitting them to sampling estimates. *Journal of soil Science*, 37(4), 617-639.
- 994 McBride, J. L., & Ebert, E. E. (2000). Verification of quantitative precipitation forecasts from
 995 operational numerical weather prediction models over Australia. *Weather and Forecasting*,
 996 15(1), 103-121.
- 997 McKee, J. L., & Binns, A. D. (2016). A review of gauge–radar merging methods for quantitative
 998 precipitation estimation in hydrology. *Canadian Water Resources Journal/Revue canadienne des*
 999 *ressources hydriques*, 41(1-2), 186-203. <https://doi.org/10.1080/07011784.2015.1064786>
- 1000 Milly, P. C. D., Wetherald, R. T., Dunne, K. A., & Delworth, T. L. (2002). Increasing risk of
 1001 great floods in a changing climate. *Nature*, 415(6871), 514-517. <https://doi.org/10.1038/415514a>
- 1002 Mockler, E. M., Chun, K. P., Sapriza-Azuri, G., Bruen, M., & Wheeler, H. S. (2016). Assessing
 1003 the relative importance of parameter and forcing uncertainty and their interactions in conceptual
 1004 hydrological model simulations. *Advances in Water Resources*, 97, 299-313.
 1005 <https://doi.org/10.1016/j.advwatres.2016.10.008>
- 1006 Mtibaa, S., & Asano, S. (2022). Hydrological evaluation of radar and satellite gauge-merged
 1007 precipitation datasets using the SWAT model: Case of the Terauchi catchment in Japan. *Journal*
 1008 *of Hydrology: Regional Studies*, 42, 101134. <https://doi.org/10.1016/j.ejrh.2022.101134>
- 1009 Nanding, N., Rico-Ramirez, M. A., & Han, D. (2015). Comparison of different radar-rain gauge
 1010 rainfall merging techniques. *Journal of Hydroinformatics*, 17(3), 422-445.
 1011 <https://doi.org/10.2166/hydro.2015.001>
- 1012 Nogueira, M., and Barros, A.P., (2015): Transient Stochastic Downscaling of Quantitative
 1013 Precipitation Estimates for Hydrological Applications. *J. Hydrology*, No. 529, 1407- [1421](https://doi.org/10.1016/j.jhydrol.2015.08.041).
 1014 <https://doi.org/10.1016/j.jhydrol.2015.08.041>.
- 1015 Oliver, M. A., & Webster, R. (2015). *Basic steps in geostatistics: the variogram and kriging*
 1016 (Vol. 106). Cham, Switzerland: Springer International Publishing.
- 1017 Penna, D., Tromp-van Meerveld, H. J., Gobbi, A., Borga, M., & Dalla Fontana, G. (2011). The
 1018 influence of soil moisture on threshold runoff generation processes in an alpine headwater



- 1019 catchment. *Hydrology and Earth System Sciences*, 15(3), 689-702. [https://doi.org/10.5194/hess-](https://doi.org/10.5194/hess-15-689-2011)
- 1020 [15-689-2011](https://doi.org/10.5194/hess-15-689-2011)
- 1021 Pielke, R. A., & Downton, M. W. (2000). Precipitation and damaging floods: Trends in the
- 1022 United States, 1932–97. *Journal of climate*, 13(20), 3625-3637. [https://doi.org/10.1175/1520-](https://doi.org/10.1175/1520-0442(2000)013<3625:PADFTI>2.0.CO;2)
- 1023 [0442\(2000\)013<3625:PADFTI>2.0.CO;2](https://doi.org/10.1175/1520-0442(2000)013<3625:PADFTI>2.0.CO;2)
- 1024 Prat, O. P., & Barros, A. P. (2010a). Assessing satellite-based precipitation estimates in the
- 1025 Southern Appalachian mountains using rain gauges and TRMM PR. *Advances in*
- 1026 *Geosciences*, 25, 143-153. <https://doi.org/10.5194/adgeo-25-143-2010>
- 1027 Prat, O. P., & Barros, A. P. (2010b). Ground observations to characterize the spatial gradients
- 1028 and vertical structure of orographic precipitation–Experiments in the inner region of the Great
- 1029 Smoky Mountains. *Journal of Hydrology*, 391(1-2), 141-156.
- 1030 <https://doi.org/10.1016/j.jhydrol.2010.07.013>
- 1031 Rafieeinassab, A., Norouzi, A., Seo, D. J., & Nelson, B. (2015). Improving high-resolution
- 1032 quantitative precipitation estimation via fusion of multiple radar-based precipitation products.
- 1033 *Journal of Hydrology*, 531, 320-336. <https://doi.org/10.1016/j.jhydrol.2015.04.066>
- 1034 Schiemann, R., Erdin, R., Willi, M., Frei, C., Berenguer, M., & Sempere-Torres, D. (2011).
- 1035 Geostatistical radar-rain gauge combination with nonparametric correlograms: methodological
- 1036 considerations and application in Switzerland. *Hydrology and Earth System Sciences*, 15(5),
- 1037 1515-1536. <https://doi.org/10.5194/hess-15-1515-2011>
- 1038 Schumacher, R. S. (2017). Heavy rainfall and flash flooding. In *Oxford research encyclopedia of*
- 1039 *natural hazard science*. <https://doi.org/10.1093/acrefore/9780199389407.013.132>
- 1040 Shao, Y., Fu, A., Zhao, J., Xu, J., & Wu, J. (2021). Improving quantitative precipitation
- 1041 estimates by radar-rain gauge merging and an integration algorithm in the Yishu River
- 1042 catchment, China. *Theoretical and Applied Climatology*, 144, 611-623.
- 1043 <https://doi.org/10.1007/s00704-021-03526-y>
- 1044 Sideris, I. V., Gabella, M., Erdin, R., & Germann, U. (2013). Real-time radar–rain-gauge
- 1045 merging using spatio-temporal co-kriging with external drift in the alpine terrain of Switzerland.
- 1046 *Quarterly Journal of the Royal Meteorological Society*, 140(680), 1097-1111.
- 1047 <https://doi.org/10.1002/qj.2188>
- 1048 Silvestro, F., Rossi, L., Campo, L., Parodi, A., Fiori, E., Rudari, R., & Ferraris, L. (2019).
- 1049 Impact-based flash-flood forecasting system: Sensitivity to high resolution numerical weather
- 1050 prediction systems and soil moisture. *Journal of Hydrology*, 572, 388-402.
- 1051 <https://doi.org/10.1016/j.jhydrol.2019.02.055>
- 1052 Smith, J. A., Baeck, M. L., Ntelekos, A. A., Villarini, G., & Steiner, M. (2011). Extreme rainfall
- 1053 and flooding from orographic thunderstorms in the central Appalachians. *Water Resources*
- 1054 *Research*, 47(4). <https://doi.org/10.1029/2010WR010190>
- 1055 Špitalar, M., Gourley, J. J., Lutoff, C., Kirstetter, P. E., Brilly, M., & Carr, N. (2014). Analysis of
- 1056 flash flood parameters and human impacts in the US from 2006 to 2012. *Journal of hydrology*,
- 1057 519, 863-870. Tao, K., and Barros, A.P., 2010: Fractal Downscaling of Satellite Precipitation
- 1058 Products for Hydrometeorological Applications. *J. Atmos. Oceanic Technol.*, 27 (3), 409-427.
- 1059 <https://doi.org/10.1175/2009JTECHA1219.1>



- 1060 Tao, J., & Barros, A. P. (2013). Prospects for flash flood forecasting in mountainous regions—An
 1061 investigation of Tropical Storm Fay in the Southern Appalachians. *Journal of Hydrology*, 506,
 1062 69-89. <https://doi.org/10.1016/j.jhydrol.2013.02.052>
- 1063 Tao, J., & Barros, A. P. (2014). Coupled prediction of flood response and debris flow initiation
 1064 during warm-and cold-season events in the Southern Appalachians, USA. *Hydrology and Earth
 1065 System Sciences*, 18(1), 367-388. <https://doi.org/10.5194/hess-18-367-2014>
- 1066 Tao, J., Wu, D., Gourley, J., Zhang, S. Q., Crow, W., Peters-Lidard, C., & Barros, A. P. (2016).
 1067 Operational hydrological forecasting during the IPHEX-IOP campaign—Meet the
 1068 challenge. *Journal of hydrology*, 541, 434-456. <https://doi.org/10.1016/j.jhydrol.2016.02.019>
- 1069 Tao, J., & Barros, A. P. (2018). Multi-year atmospheric forcing datasets for hydrologic modeling
 1070 in regions of complex terrain—Methodology and evaluation over the Integrated Precipitation and
 1071 Hydrology Experiment 2014 domain. *Journal of Hydrology*, 567, 824-842.
 1072 <https://doi.org/10.1016/j.jhydrol.2016.12.058>
- 1073 Tao, J., and Barros, A.P., 2019: Multi-Year Surface Radiative Properties and Vegetation
 1074 Parameters for Hydrologic Modeling in Regions of Complex Terrain – Methodology and
 1075 Evaluation over the IPHEX2014 Domain. *J. Hydrology-Reg. Studies*, 22, e100596. <https://doi.org/10.1016/j.ejrh.2019.100596>.
- 1076
- 1077 Troch, P. A., Smith, J. A., Wood, E. F., & de Troch, F. P. (1994). Hydrologic controls of large
 1078 floods in a small basin: central Appalachian case study. *Journal of Hydrology*, 156(1-4), 285-
 1079 309. [https://doi.org/10.1016/0022-1694\(94\)90082-5](https://doi.org/10.1016/0022-1694(94)90082-5)
- 1080 Uber, M., Vandervaere, J. P., Zin, I., Braud, I., Heistermann, M., Legoût, C., ... & Nord, G.
 1081 (2018). How does initial soil moisture influence the hydrological response? A case study from
 1082 southern France. *Hydrology and Earth System Sciences*, 22(12), 6127-6146.
 1083 <https://doi.org/10.5194/hess-22-6127-2018>
- 1084 Vignal, B., Galli, G., Joss, J., & Germann, U. (2000). Three methods to determine profiles of
 1085 reflectivity from volumetric radar data to correct precipitation estimates. *Journal of Applied
 1086 Meteorology and Climatology*, 39(10), 1715-1726. <https://doi.org/10.1175/1520-0450-39.10.1715>
- 1087
- 1088 Villarini, G., & Krajewski, W. F. (2010). Review of the different sources of uncertainty in single
 1089 polarization radar-based estimates of rainfall. *Surveys in geophysics*, 31, 107-129.
 1090 <https://doi.org/10.1007/s10712-009-9079-x>
- 1091 Vivoni, E. R., Entekhabi, D., Bras, R. L., & Ivanov, V. Y. (2007). Controls on runoff generation
 1092 and scale-dependence in a distributed hydrologic model. *Hydrology and Earth System Sciences*,
 1093 11(5), 1683-1701. <https://doi.org/10.5194/hess-11-1683-2007>
- 1094 Wang, K. H., Chu, T., Yang, M. D., & Chen, M. C. (2020). Geostatistical based models for the
 1095 spatial adjustment of radar rainfall data in typhoon events at a high-elevation river watershed.
 1096 *Remote Sensing*, 12(9), 1427. <https://doi.org/10.3390/rs12091427>
- 1097 Wang, J., & Wolff, D. B. (2010). Evaluation of TRMM ground-validation radar-rain errors using
 1098 rain gauge measurements. *Journal of Applied Meteorology and Climatology*, 49(2), 310-324.



- 1099 Weiland, F. C. S., Vrugt, J. A., Weerts, A. H., & Bierkens, M. F. (2015). Significant uncertainty
 1100 in global scale hydrological modeling from precipitation data errors. *Journal of Hydrology*, 529,
 1101 1095–1115. <https://doi.org/10.1016/j.jhydrol.2015.08.061>
- 1102 Wehbe, Y., Temimi, M., & Adler, R. F. (2020). Enhancing precipitation estimates through the
 1103 fusion of weather radar, satellite retrievals, and surface parameters. *Remote Sensing*, 12(8), 1342.
 1104 <https://doi.org/10.3390/rs12081342>
- 1105 Wernberg, T., Smale, D., Tuya, F., Thomsen, M. S., Langlois, T. J., de Bettignies, T., Bennett,
 1106 S., & Rousseaux, C. S. (2013). An extreme climatic event alters marine ecosystem structure in a
 1107 global biodiversity hotspot. *Nature Climate Change*, 3, 78–82.
 1108 <https://doi.org/10.1038/nclimate1627>
- 1109 Wilson, A. M., & Barros, A. P. (2014). An investigation of warm rainfall microphysics in the
 1110 southern Appalachians: Orographic enhancement via low-level seeder–feeder
 1111 interactions. *Journal of the Atmospheric Sciences*, 71(5), 1783–1805.
 1112 <https://doi.org/10.1175/JAS-D-13-0228.1>
- 1113 Wolvin, S., Strong, C., Rupper, S., & Steenburgh, W. J. (2024). Climatology of orographic
 1114 precipitation gradients over High Mountain Asia derived from dynamical downscaling. *Journal*
 1115 *of Geophysical Research: Atmospheres*, 129(20), e2024JD041010.
 1116 <https://doi.org/10.1029/2024JD041010>
- 1117 Yildiz, O., & Barros, A. P. (2004). Climate variability, water resources, and hydrologic
 1118 extremes—Modeling the water and energy budgets. In *Climate and Hydrology in Mountain*
 1119 *Areas*, (Eds. C. de Jong, D. Collins, and R. Ranzi), John Wiley and Sons (Pub.) , 303–318.
 1120 <https://doi.org/10.1002/0470858249.ch20>
- 1121 Yildiz, O., & Barros, A. P. (2007). Elucidating vegetation controls on the hydroclimatology of a
 1122 mid-latitude basin. *Journal of Hydrology*, 333(2–4), 431–448.
 1123 <https://doi.org/10.1016/j.jhydrol.2006.09.010>
- 1124 Yildiz, O., & Barros, A. P. (2009). Evaluating spatial variability and scale effects on hydrologic
 1125 processes in a midsize river basin. *Sci. Res. Essays*, 4, 217–225.
 1126 <https://doi.org/10.5897/SRE.9000465>
- 1127 Zappa, M., Jaun, S., Germann, U., Walser, A., & Fundel, F. (2011). Superposition of three
 1128 sources of uncertainties in operational flood forecasting chains. *Atmospheric Research*, 100(2–3),
 1129 246–262. <https://doi.org/10.1016/j.atmosres.2010.12.005>
- 1130 Zehe, E., & Blöschl, G. (2004). Predictability of hydrologic response at the plot and catchment
 1131 scales: Role of initial conditions. *Water Resources Research*, 40(10).
- 1132 Zhang, J., Howard, K., Langston, C., Kaney, B., Qi, Y., Tang, L., Grams, H., Wang, Y., Cocks,
 1133 S., Martinaitis, S., Arthur, A., Cooper, K., Brogden, J., & Kitzmiller, D. (2016). Multi-radar
 1134 multi-sensor (MRMS) quantitative precipitation estimation: Initial operating capabilities
 1135 [Dataset]. *Bulletin of the American Meteorological Society*, 97(4), 621–638.
 1136 <https://doi.org/10.1175/BAMS-D-14-00174.1>
- 1137 Zhang, X., & Anagnostou, E. N. (2019). Evaluation of numerical weather model–based satellite
 1138 precipitation adjustment in tropical mountainous regions. *Journal of Hydrometeorology*, 20(3),
 1139 431–445. <https://doi.org/10.1175/JHM-D-18-0008.1>



1140 Zhang, Y., Schaap, M. G., & Zha, Y. (2018). A high-resolution global map of soil hydraulic
1141 properties produced by a hierarchical parameterization of a physically based water retention
1142 model. *Water Resources Research*, 54(12), 9774-9790. <https://doi.org/10.1029/2018WR023539>
1143 Zimmerman, D. L., & Zimmerman, M. B. (1991). A comparison of spatial semivariogram
1144 estimators and corresponding ordinary kriging predictors. *Technometrics*, 33(1), 77-91.
1145 <https://doi.org/10.1080/00401706.1991.10484771>
1146
1147
1148



LIST OF TABLES

Table 1 - Raingauge index and exact locations as illustrated in Figure 1. Two rain gauges highlighted in bold font are installed at Purchase Knob, a supersite in the inner mountain region. Locations equipped with more than one raingauge (collocated) are shaded in grey color, and these collocated raingauges generally differ in tipping sizes. This table is adapted from Liao and Barros (2019).

Table 2 - Hydrologic skills used in this work.

Table 3 - Information table for selected basins and corresponding streamflow gauges used in this work. This table is adapted from Liao and Barros (2025b).



Table 1 – Raingauge index and exact locations as illustrated in Figure 1. Two rain gauges highlighted in bold font are installed at Purchase Knob, a supersite in the inner mountain region. Locations equipped with more than one raingauge (collocated) are shaded in grey color, and these collocated raingauges generally differ in tipping sizes. This table is adapted from Liao and Barros (2019).

NO.	Site ID.	Latitude	Longitude	Elevation (m)
01	RG 001	35.398	-82.913	1156
02	RG 002	35.417	-82.971	1731
03	RG 003	35.384	-82.916	1609
04	RG 004	35.368	-82.990	1922
05	RG 005	35.408	-82.964	1520
06	RG 008	35.382	-82.973	1737
07	RG 010	35.456	-82.946	1478
08	RG 100	35.586	-83.072	1495
09	RG 100T	35.587	-83.064	1485
10	RG 101	35.575	-83.088	1520
11	RG 102	35.563	-83.103	1635
12	RG 103	35.553	-83.117	1688
13	RG 104	35.554	-83.088	1584
14	RG 106	35.432	-83.029	1210
15	RG 109	35.495	-83.040	1500
16	RG 110	35.548	-83.148	1563
17	RG 300	35.726	-83.216	1558
18	RG 301	35.705	-83.255	2003
19	RG 302	35.721	-83.246	1860
20	RG 303PK	35.586	-83.072	1495
21	RG 303S	35.762	-83.162	1490
22	RG 304	35.670	-83.182	1820
23	RG 305	35.691	-83.131	1630
24	RG 306	35.745	-83.171	1536
25	RG 307	35.651	-83.199	1624
26	RG 308	35.730	-83.182	1471
27	RG 309	35.682	-83.150	1604
28	RG 310	35.702	-83.122	1756
29	RG 311	35.765	-83.140	1036
30	RG 400	35.702	-83.122	1756
31	RG 401	35.651	-83.199	1624
32	RG 402	35.721	-83.246	1860
33	RG 403	35.517	-83.101	925
34	RG 407	35.517	-83.101	925



1169 **Table 2:** Hydrologic skills used in this work.

Notation	Information	Reference
KGE	Kling-Gupta efficiency	Eq. (19) /Gupta et al. (2009)
EV	Relative error in flood volume	Eq. (20)
EPT	Error in peak flow timing	Flood front timing differences
EPV	Relative Error in maximum flow rate	Eq. (21)

1170



Table 3 – Information table for selected basins and corresponding streamflow gauges used in this work. This table is adapted from Liao and Barros (2025b).

Basin index	USGS Gauge ID	Drainage area (km ²)	Basin highest elevation (m)	Basin relief (m)	Location
1	3544970	118.7	1442	847	GA
2	2178400	176.1	1629	1051	GA
3	3504000	149.9	1667	1032	NC
4	3497300	317.6	1999	1651	TN
5	3460000	148.1	1879	1174	NC
6	3456500	152.8	1873	1157	NC
8	344894205	41.3	1995	1221	NC
9	3463300	134.3	1989	1425	NC
10	3400500	234.7	1257	1257	KY
11	3479000	283.3	1772	1216	NC
13	3182700	447.3	1111	717	WV
14	2011460	194.4	1388	763	VA
15	1620500	54.5	1321	712	VA
16	3180500	426.8	1416	621	WV
17	3068800	437.1	1471	908	WV
18	1595000	234.8	1230	560	MD
19	1595300	130.3	1069	712	WV
20	1544500	445.9	765	457	PA
21	1422747	81.4	766	394	NY
22	1415000	106.8	1019	636	NY
23	1413398	152.8	1094	754	NY
24	13621955	41.7	1074	717	NY
25	1421610	51.3	970	497	NY
26	1074520	389.4	1582	1582	NH
27	10642505	294.9	1895	1693	NH
28	1137500	300.3	1894	1546	NH
29	1133000	183.2	975	719	VT
30	1055000	334.1	1143	975	MAINE



LIST OF FIGURES

Figure 1 - Map of IPHEX (Barros et al., 2014) ground-based observations in the Southern Appalachians. Raingauge is denoted as a character string starting with three-digit number potentially followed by extra letters; locations started with a letter P represent disdrometers. The basic information regarding these stations is listed in Table 1. This figure is adapted from Liao and Barros (2019).

Figure 2 – Workflow to generate the product $STIV_{DBKC}$.

Figure 3 – An illustration of the structure of IRC, ICC and the coupled IRC-ICC framework including **a)** the residual hydrograph between the observed and simulated discharge, with the discharge water difference $wd(t)$ being distributed across the time window T ; **b)** Example of travel time distribution $TT(t)$ and map (inset) illustrating a hypothetical distribution of runoff source areas (in red, $ns=3$) with travel time x_2 contributing to streamflow at time t , meaning that at time $t-x_2$ there are three pixels ($ns=3$) generating runoff that reaches the outlet at time t . T is the time window over which runoff source areas with $TT < T$ are mapped and the inverse rainfall correction (IRC) are applied; **c)** Example of IRC windows guided by timescales of dominant hydrological processes. The first window solely covers the initial streamflow conditions before the target event. The second window depicts the early rising limb of the hydrograph. The third window captures the steep rising limb of the hydrograph until it reaches the peak flow. The fourth and fifth windows correspond to interflow-dominant and baseflow-dominant stages of the recession curve respectively, separated by the recession inflection point; **d)** A schematic drawing that shows different characteristic timings in a hydrograph with the implementation of the Initial Condition Correction (ICC) strategy. Specifically, T_{r*} and T_r represent the timing of flood front in simulations and observations, respectively. T_p is the timing of observed maximum flood. The inflection point of the recession curve of the observations is denoted as T_I . Flow differences at t_1 and t_2 are denoted as ΔS_1 and ΔS_2 respectively for the purpose of discussion. P , Q and IC represent precipitation, flow discharge and initial condition, respectively; **e)** The implemented framework in this work consisting of ICC and IRC. This figure is adapted from Liao and Barros (2022, 2025b).

Figure 4 – Map of the Continental United States (CONUS) and headwater basins studied in this work. Basin information is available in Table 3. Sub-regions are delineated as the following for discussion purposes only: Northern, Central and Southern Appalachian Mountains (NAM, Basin 21-30; CAM, Basin 13-20; SAM, Basin 01-11). This figure is adapted from Liao and Barros (2025b).

Figure 5 - Examples of raingauge measurements showing the diurnal cycle of different seasons at different locations: Left panel – raingauge RG008 located in the eastern ridges for the Summer (JAS: July-August-September) season. Right panel – raingauge RG302 located in the western ridges for the Spring (AMJ; April-May-June) season. Rain gauge measurements (blue); StageIV_{DBK} (black); StageIV_{DBKC} (green). This figure is from Liao and Barros (2019).

Figure 6 –Top row – The diurnal cycle of missing precipitation at RG003 (Eastern ridges) and RG103 (Inner regions) for January-February-March (JFM) using various products. Bottom row-corresponding rain gauge climatology (blue). StageIV_D (black); StageIV_{DBK} (cyan); StageIV_{DBKC} (green). This figure is from Liao and Barros (2019).



Figure 7 – Statistical evaluation summary for winter precipitation (JFM, January, February, and March): a) Diurnal cycle of mean HSS and TS statistics including all rain gauges calculated using all data from 2008 to 2017: $STIV_D$ (black) and $STIV_{DBKC}$ (green); b) HSS and TS statistics calculated using different rain rate thresholds over the same 10-year period; c) Diurnal cycle of rain rate RMSE at seasonal-scale, and its dependence on observed rainfall rate. This figure is from Liao and Barros (2019).

Figure 8 – The IRC-ICC performance in Basin05 as an example for the 2017-10-23 event (Basin05: Cataloochee Creek Basin, NC). This event is part of the 2017 Hurricane Nate. This figure contains a) hydrological responses when precipitation forcing is the $STIV_{DBKC}$. The dashed rectangular plot consisting of intermediate results including each iteration from the IRC-ICC framework (Figure 3). b) the hydrological equilibrium of the IRC-ICC after 5 iterations. This figure is adapted from Liao and Barros (2025b).

Figure 9 – The IRC-ICC performance for different subregions, include a) 3 events from the Southern Appalachians; b) 3 events from the Central Appalachians; and c) 3 events from the Northern Appalachians. The IRC-ICC KGE evolution plots from iterations are included below the hydrographs. The black and pink line are from the original $STIV_D$ and the IRC-ICC equilibrium state ($STIV_D^{IRC*}$), respectively, and KGE values are displayed as colored numbers in the top left corners. This figure is adapted from Liao and Barros (2025b).

Figure 10 – Event total precipitation maps for three cold season events (a) and three warm season events (b). Each column represents one event, and each row represents one precipitation product: $STIV_{DBKC}$, $STIV_{DBKC}^{IRC*}$ from IRC-only framework, and $STIV_{DBKC}^{IRC*}$ from the coupled IRC-ICC framework. This figure is adapted from Liao and Barros (2025b).

Figure 11 – Summary charts of precipitation statistics for all event-total precipitation maps. Basin precipitation average and standard deviation for each event are represented by circles and triangles in the top and bottom panel, respectively. Each panel consists of 3 sub-regions by vertical black lines: the Southern Appalachian Mountains, Central Appalachian Mountains, and Northern Appalachian Mountains. The list of events in Basin 05 (with event number ranging from 55 to 108) in the SAM is highlighted by a blue rectangle for further discussion in the text. The average values of all events for both the mean and the standard deviation are calculated and shown in the top right corner. Black color and pink color represent pre and post IRC-ICC QPE statistics, respectively.

Figure 12 – Summary of hydrologic skills. Green dashed lines and associated uncertainty envelopes are only for visual illustration. Hydrologic statistics are explained in Table 2. Pink and black scatters (each scatter represent one event) represent IRC-ICC, and baseline outputs, respectively. Each horizontal panel is split into 3 subsections by vertical black lines representing the 3 subregions. Histograms graphs on the right hand side are provided for a summary view. This figure is adapted from Liao and Barros (2025b).

Figure 13 – a) Event total QPE plots for various QPE datasets conditional on seasons and KGE values; b) KGE distributions across events using different QPE datasets. This figure is adapted from Liao and Barros (2025b).

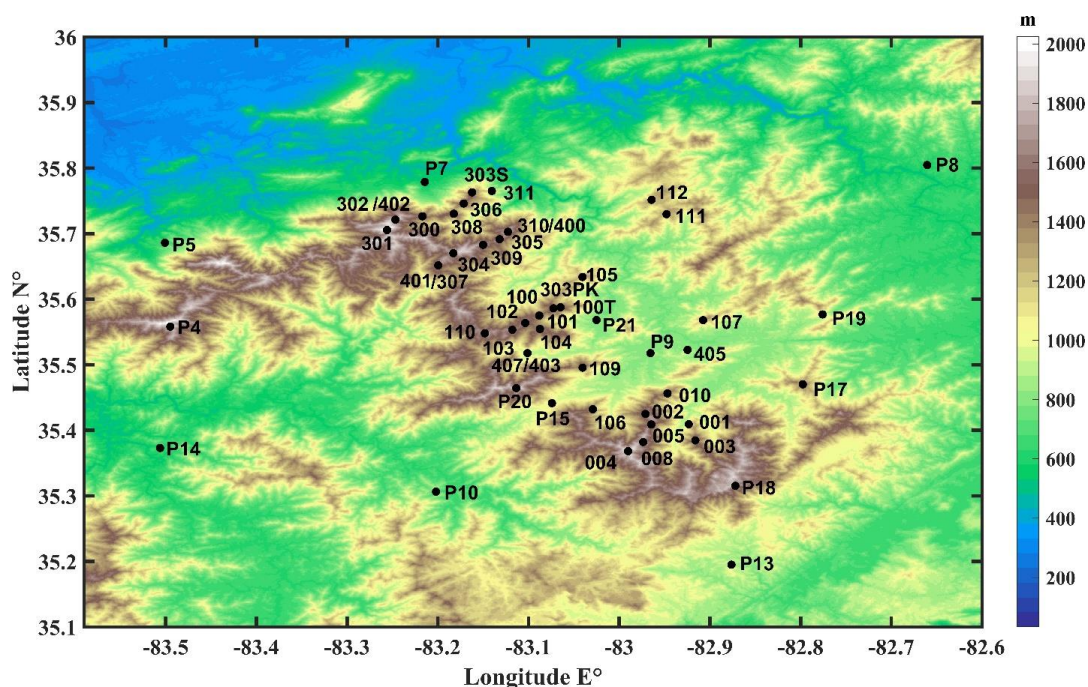


Figure 1 - Map of IPHEX (Barros et al., 2014) ground-based observations in the Southern Appalachians. Raingauge is denoted as a character string starting with three-digit number potentially followed by extra letters; locations started with a letter P represent disdrometers. The basic information regarding these stations is listed in Table 1. This figure is adapted from Liao and Barros (2019).

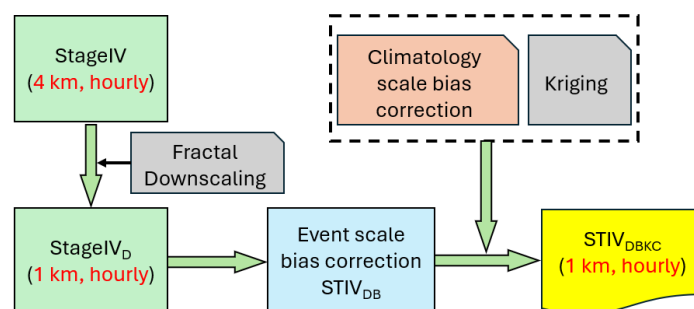


Figure 2 – Workflow to generate the product $STIV_{DBKC}$.

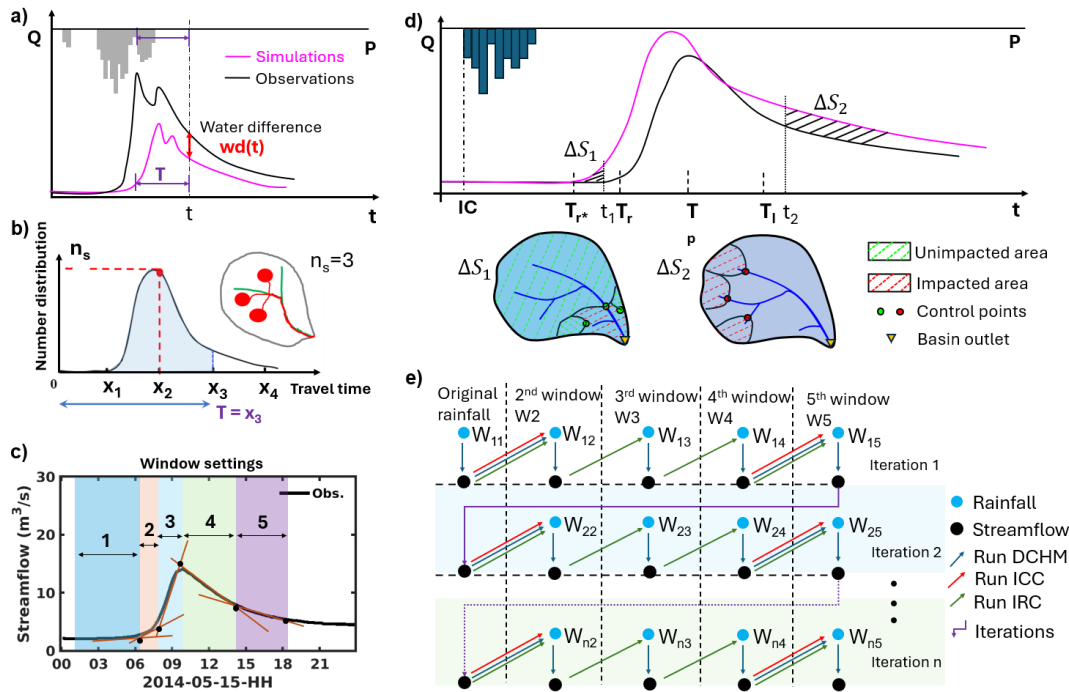


Figure 3 – An illustration of the structure of IRC, ICC and the coupled IRC-ICC framework including **a)** the residual hydrograph between the observed and simulated discharge, with the discharge water difference $wd(t)$ being distributed across the time window T ; **b)** Example of travel time distribution $TT(t)$ and map (inset) illustrating a hypothetical distribution of runoff source areas (in red, $n_s=3$) with travel time x_2 contributing to streamflow at time t , meaning that at time $t-x_2$ there are three pixels ($n_s=3$) generating runoff that reaches the outlet at time t . T is the time window over which runoff source areas with $TT < T$ are mapped and the inverse rainfall correction (IRC) are applied; **c)** Example of IRC windows guided by timescales of dominant hydrological processes. The first window solely covers the initial streamflow conditions before the target event. The second window depicts the early rising limb of the hydrograph. The third window captures the steep rising limb of the hydrograph until it reaches the peak flow. The fourth and fifth windows correspond to interflow-dominant and baseflow-dominant stages of the recession curve respectively, separated by the recession inflection point; **d)** A schematic drawing that shows different characteristic timings in a hydrograph with the implementation of the Initial Condition Correction (ICC) strategy. Specifically, T_{r*} and T_r represent the timing of flood front in simulations and observations, respectively. T_p is the timing of observed maximum flood. The inflection point of the recession curve of the observations is denoted as T_I . Flow differences at t_1 and t_2 are denoted as ΔS_1 and ΔS_2 respectively for the purpose of discussion. P , Q and IC represent precipitation, flow discharge and initial condition, respectively; **e)** The implemented framework in this work consisting of ICC and IRC. This figure is adapted from Liao and Barros (2022, 2025b).

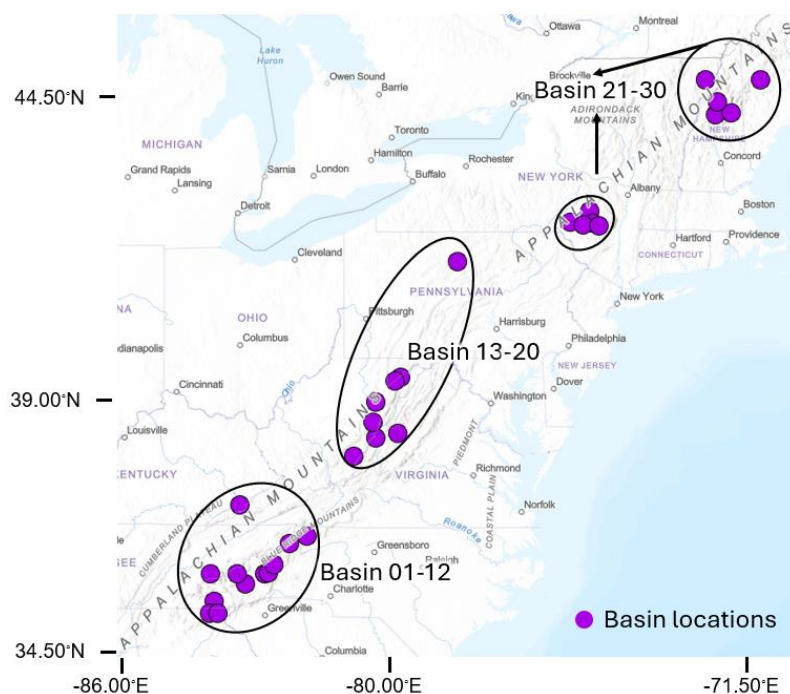


Figure 4 – Map of the Continental United States (CONUS) and headwater basins studied in this work. Basin information is available in Table 3. Sub-regions are delineated as the following for discussion purposes only: Northern, Central and Southern Appalachian Mountains (NAM, Basin 21-30; CAM, Basin 13-20; SAM, Basin 01-11). This figure is adapted from Liao and Barros (2025b).

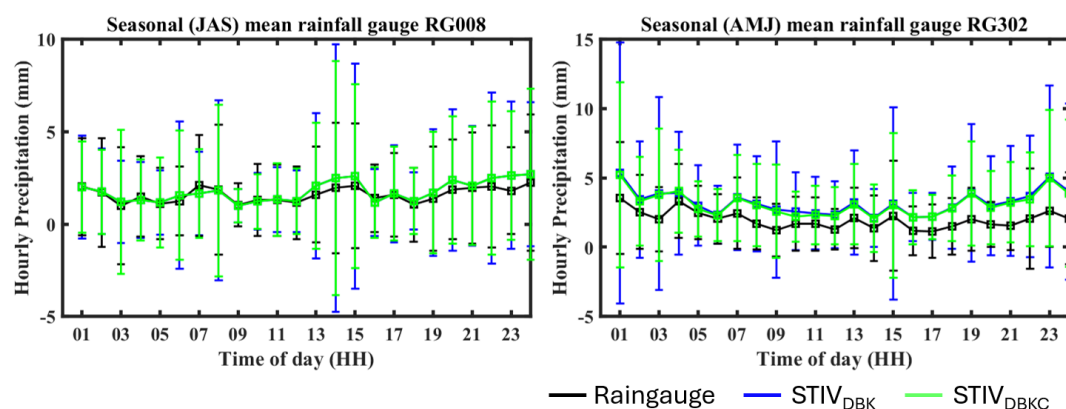


Figure 5 – Examples of raingauge measurements showing the diurnal cycle of different seasons at different locations: Left panel – raingauge RG008 located in the eastern ridges for the Summer (JAS: July-August-September) season. Right panel – raingauge RG302 located in the western ridges for the Spring (AMJ; April-May-June) season. Rain gauge measurements (blue); StageIV_{DBK} (black); StageIV_{DBKc} (green). This figure is from Liao and Barros (2019).

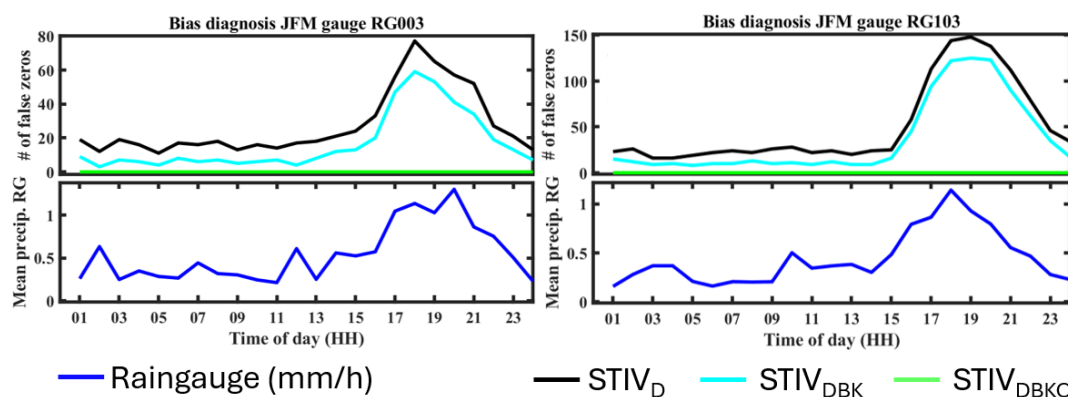
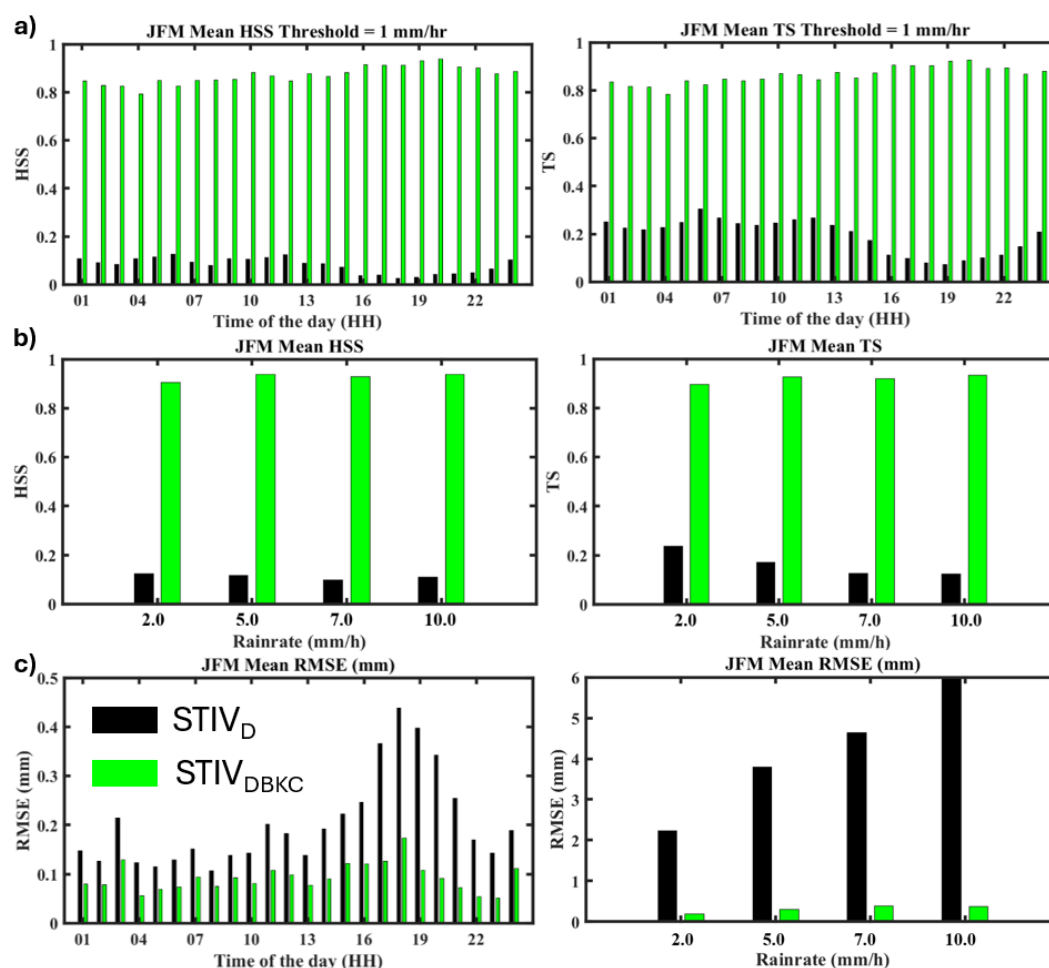


Figure 6 –Top row – The diurnal cycle of missing precipitation at RG003 (Eastern ridges) and RG103 (Inner regions) for January-February-March (JFM) using various products. Bottom row- corresponding rain gauge climatology (blue). StageIV_D (black); StageIV_{DBK} (cyan); StageIV_{DBKc} (green). This figure is from Liao and Barros (2019).

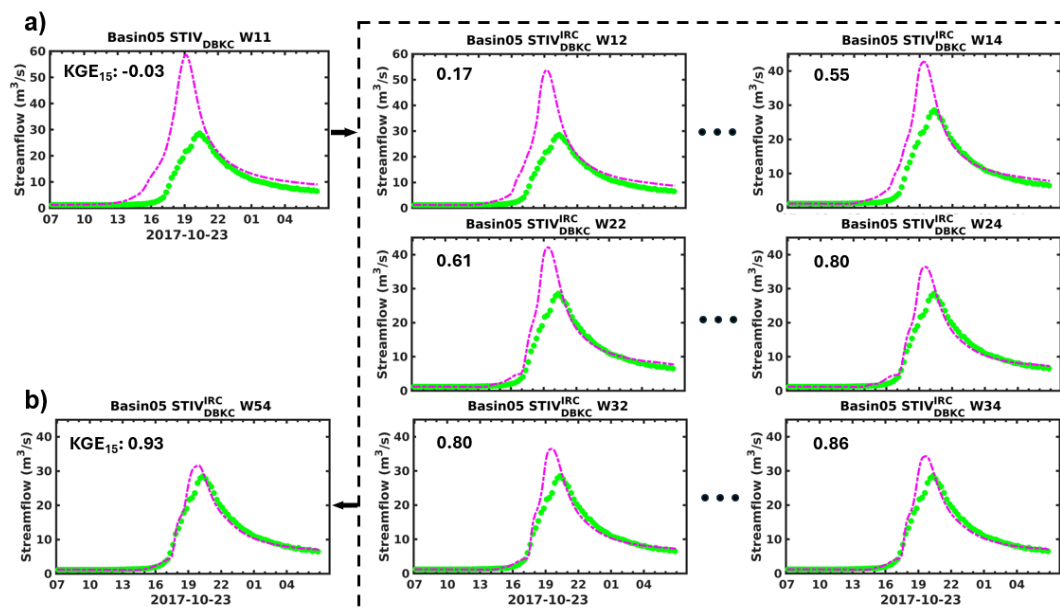


1310



1311

1312 **Figure 7** – Statistical evaluation summary for winter precipitation (JFM, January, February, and
 1313 March): a) Diurnal cycle of mean HSS and TS statistics including all rain gauges calculated using
 1314 all data from 2008 to 2017: STIV_D (black) and STIV_{DBK} (green); b) HSS and TS statistics
 1315 calculated using different rain rate thresholds over the same 10-year period; c) Diurnal cycle of
 1316 rain rate RMSE at seasonal-scale, and its dependence on observed rainfall rate. This figure is from
 1317 Liao and Barros (2019).



1318

Figure 8 – The IRC-ICC performance in Basin05 as an example for the 2017-10-23 event (Basin05: Cataloochee Creek Basin, NC). This event is part of the 2017 Hurricane Nate. This figure contains **a)** hydrological responses when precipitation forcing is the $STIV_{DBKC}$. The dashed rectangular plot consisting of intermediate results including each iteration from the IRC-ICC framework (Figure 3). **b)** the hydrological equilibrium of the IRC-ICC after 5 iterations. This figure is adapted from Liao and Barros (2025b).

1325

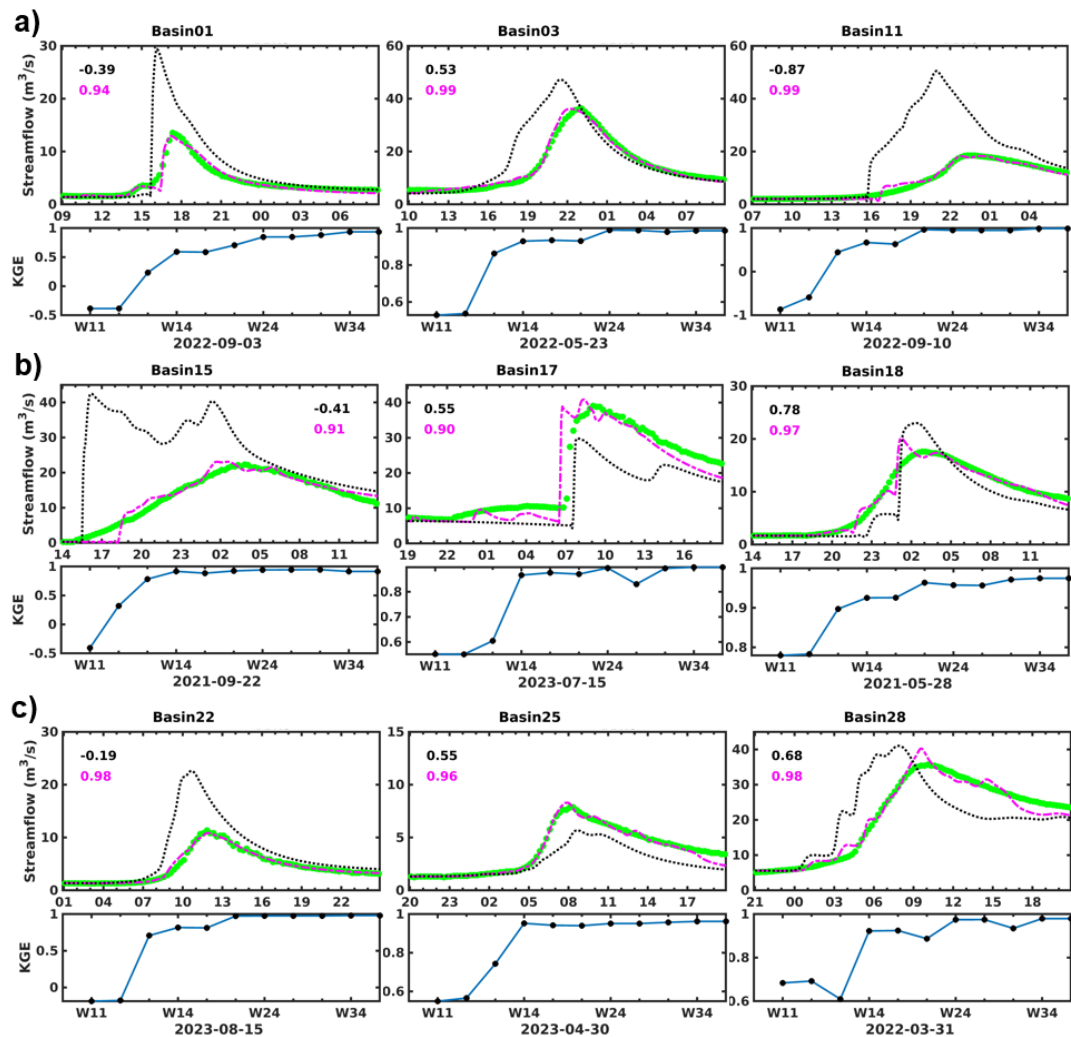
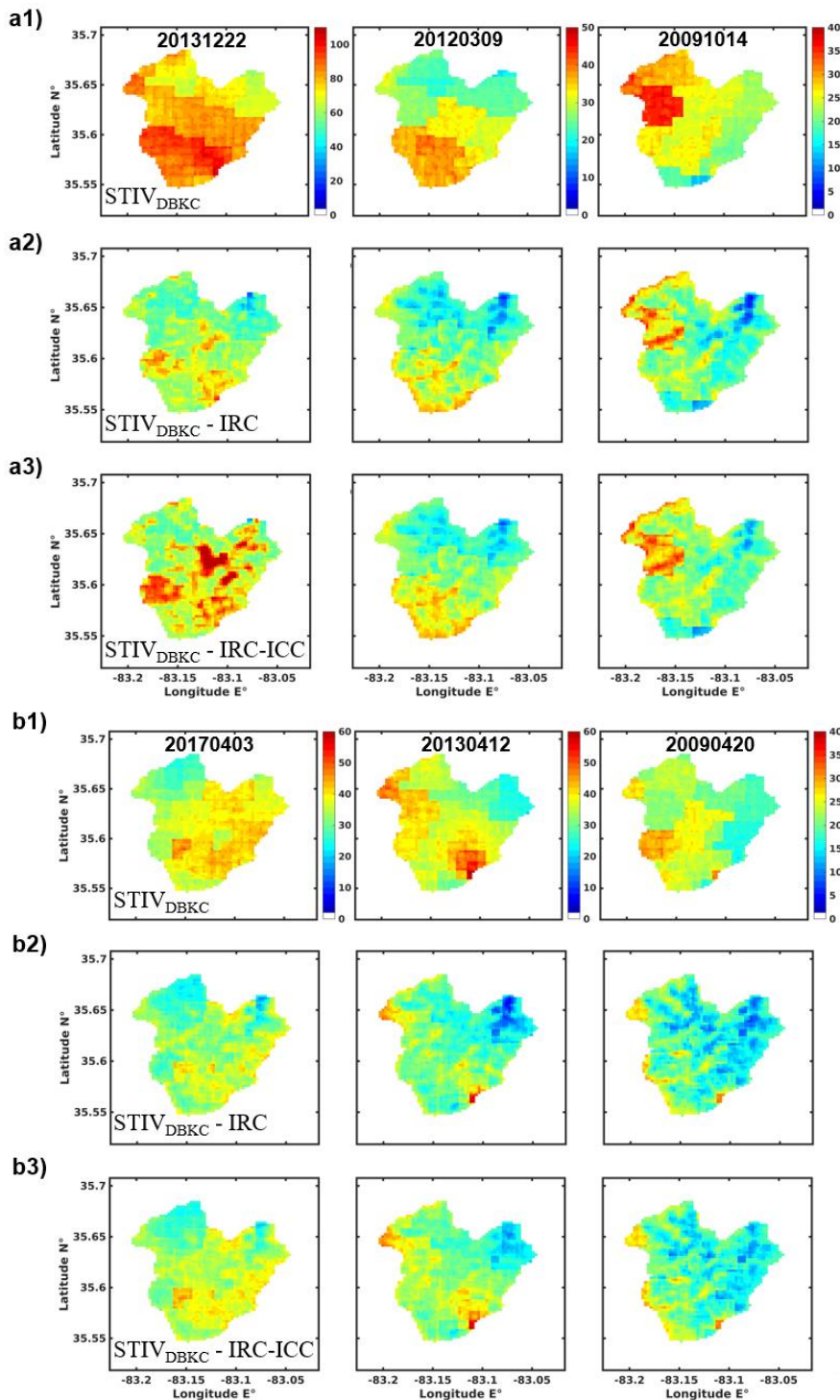


Figure 9 – The IRC-ICC performance for different subregions, include **a)** 3 events from the Southern Appalachians; **b)** 3 events from the Central Appalachians; and **c)** 3 events from the Northern Appalachians. The IRC-ICC KGE evolution plots from iterations are included below the hydrographs. The black and pink line are from the original $STIV_D$ and the IRC-ICC equilibrium state ($STIV_D^{IRC*}$), respectively, and KGE values are displayed as colored numbers in the top left corners. This figure is adapted from Liao and Barros (2025b).





1335
1336 **Figure 10** – Event total precipitation maps for three cold season events (**a**) and three warm season
1337 events (**b**). Each column represents one event, and each row represents one precipitation product:
1338 $STIV_{DBKC}$, $STIV_{DBKC}^{IRC*}$ from IRC-only framework, and $STIV_{DBKC}^{IRC*}$ from the coupled IRC-ICC
1339 framework. This figure is adapted from Liao and Barros (2025b).
1340

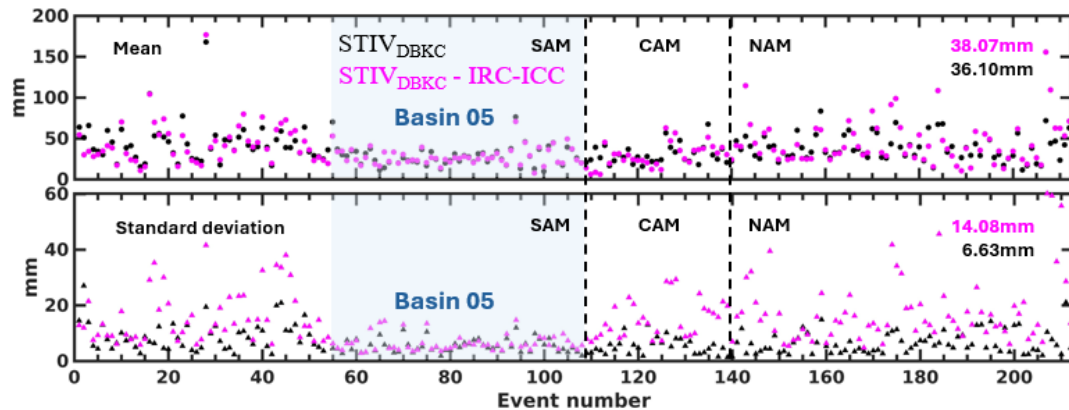


Figure 11 – Summary charts of precipitation statistics for all event-total precipitation maps. Basin precipitation average and standard deviation for each event are represented by circles and triangles in the top and bottom panel, respectively. Each panel consists of 3 sub-regions by vertical black lines: the Southern Appalachian Mountains, Central Appalachian Mountains, and Northern Appalachian Mountains. The list of events in Basin 05 (with event number ranging from 55 to 108) in the SAM is highlighted by a blue rectangle for further discussion in the text. The average values of all events for both the mean and the standard deviation are calculated and shown in the top right corner. Black color and pink color represent pre and post IRC-ICC QPE statistics, respectively.

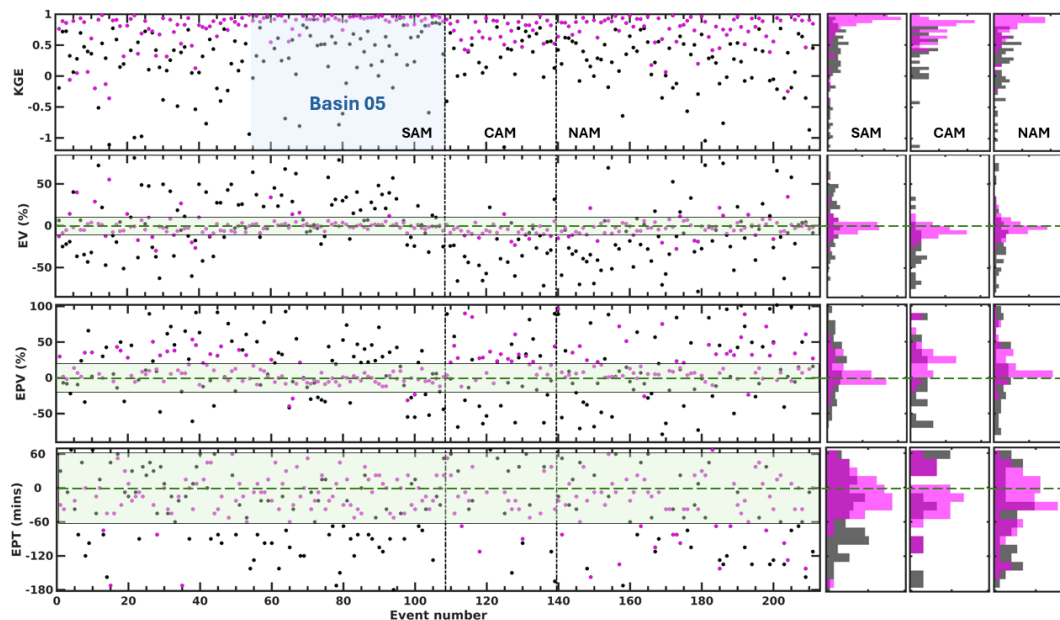
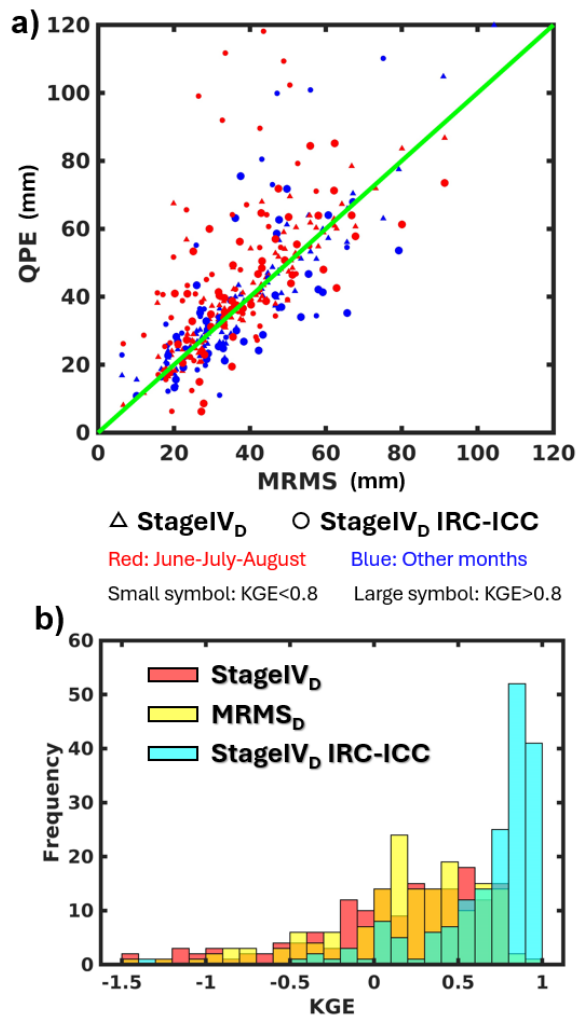


Figure 12 – Summary of hydrologic skills. Green dashed lines and associated uncertainty envelopes are only for visual illustration. Hydrologic statistics are explained in Table 2. Pink and black scatters (each scatter represent one event) represent IRC-ICC, and baseline outputs, respectively. Each horizontal panel is split into 3 subsections by vertical black lines representing the 3 subregions. Histograms graphs on the right hand side are provided for a summary view. This figure is adapted from Liao and Barros (2025b).



1362

1363 **Figure 13** – a) Event total QPE plots for various QPE datasets conditional on seasons and KGE
 1364 values; b) KGE distributions across events using different QPE datasets. This figure is adapted
 1365 from Liao and Barros (2025b).

1366